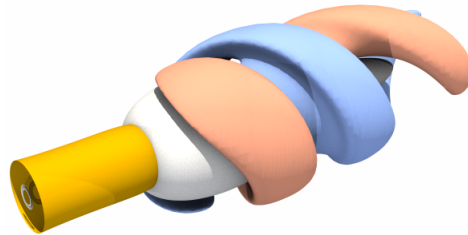


Technical University of Berlin

Institute of Fluid Dynamics and Technical Acoustics
Laboratory for Flow Instabilities and Dynamics
Prof. Dr.-Ing. K. Oberleithner



Master Thesis

Identification of Coherent Structures in Non-Reacting and Reacting Jet Flows using Spectral Proper Orthogonal Decomposition and Resolvent Analysis

Mario Casel

Berlin, den 16.06.2020

Email: mario.casel@outlook.de
Matriculation Number: 363 844
Study Program: Engineering Science M.Sc.
Supervisors: Prof. Dr.-Ing. Kilian Oberleithner(Technical University of Berlin)
Dr. -Ing. Thomas Ludwig Kaiser(Technical University of Berlin)

Erklärung der Selbstständigkeit / Declaration of Authorship

Hiermit erkläre ich, dass ich die vorliegende Arbeit selbstständig und eigenhändig sowie ohne unerlaubte fremde Hilfe und ausschließlich unter Verwendung der aufgeführten Quellen und Hilfsmittel angefertigt habe.

This thesis is composed of my original work, and contains no material previously published or written by another person except where due reference has been made in the text. I have clearly stated the contribution by others to jointly-authored works that I have included in my thesis.

Berlin, 16.06.2020



Mario Casel

Zusammenfassung

Die vorliegende Arbeit befasst sich mit der Identifizierung und Untersuchung kohärenter Strukturen in inkompressiblen, turbulenten, nicht-reagierenden und reagierenden Freistrahls-Strömungen, basierend auf einem Large-Eddy-Simulation (LES)-Datensatz. Spectral Proper Orthogonal Decomposition (SPOD) wird auf die zeit-aufgelösten Snapshot-Daten angewendet und zerlegt das Strömungsfeld in raum-zeit-kohärente Moden. Globale Resolventen-Analyse (RA), die auf den zeitlich gemittelten Strömungsfeldern beruht, ermittelt die Antwort (Response) des Strömungsfeldes auf optimale Anregung (Forcing). Der reagierende Freistrahls wird zusätzlich mittels globaler Linearer Stabilitätsanalyse (LSA) auf die Entstehungsmechanismen kohärenter Strömungsdynamik untersucht. Die Analyse des nicht-reagierenden Freistrahls basiert auf den linearisierten, inkompressiblen Navier-Stokes-Gleichungen (LNSE). Der Einfluss der Flamme wird durch eine zusätzliche Gleichung berücksichtigt, die das nicht-homogene Dichte-Feld miteinbezieht. Die daraus sogenannten linearen Low-Mach-Gleichungen dienen als Grundlage für die RA und LSA im reagierenden Strömungsszenario. Alle genannten Methoden werden im bi-globalen Framework angewendet. Axialsymmetrische, sowie helikale Analyse-Ergebnisse werden präsentiert.

Im nicht-reagierenden Freistrahls ermittelt die SPOD axialsymmetrische Moden, die als Kelvin-Helmholtz (KH)-typisch identifiziert werden und welche in relativer Betrachtung am meisten Energie im mittleren Frequenzbereich beinhalten - das sogenannte Low-Rank-Verhalten. Die RA ermittelt die gleiche Dynamik als verstärkte Antwort des mittleren Feldes auf optimale harmonische Anregung. Die Verstärkung (Gain) ist ebenfalls im mittleren Frequenzbereich verhältnismäßig am größten. Das optimale Forcing spiegelt den Orr-Mechanismus in der Grenzschicht der Hauptdüse wieder. Die Übereinstimmung zwischen helikalen SPOD- und RA-Moden ist ebenfalls gut. Low-Rank-Verhalten tritt wieder im mittleren Frequenzbereich auf, setzt sich allerdings auch in Frequenzen fort, die gegen null gehen. Die Ergebnisse aus SPOD und RA werden mit aktueller Fachliteratur verglichen und zeigen eine gute Übereinstimmung.

SPOD-Ergebnisse des reagierenden Freistrahls weisen signifikante Unterschiede im Vergleich zu den Ergebnissen der nicht-reagierenden Strömung auf. Die aus Energie-Perspektive dominantesten Moden verschieben sich vom mittleren in den niedrigen Frequenzbereich.

Das Low-Rank-Verhalten bildet sich ebenfalls wesentlich stärker aus, sodass axialsymmetrische Moden bis zu 40% der gesamten turbulenten kinetischen Energie beinhalten. Für Frequenzen die gegen null gehen, nimmt diese Dominanz, ähnlich wie im nicht-reagierenden Fall, wieder ab. Im Vergleich dazu, erhalten helikale Strukturen ihre energetische Dominanz für sehr geringe Frequenzen. Global betrachtet, ähneln die Dynamiken denen des nicht-reagierenden Strömungsszenarios.

Als Übergang zur Analyse des reagierenden Freistrahls mittels der Low-Mach-Gleichungen, wird zunächst die RA, basierend auf den LNSE für nicht-reagierende Strömungen, auf die mittleren Felder der reagierenden LES angewendet. Obwohl dieser Ansatz nicht in der gleichen Dynamik resultiert, wie sie von der SPOD ermittelt wird, betont er die Bedeutung der nicht-homogenen Dichte und motiviert somit die Analyse basierend auf den Low-Mach-Gleichungen.

Die Low-Mach-RA resultiert in der gleichen Strömungsdynamik wie sie mittels SPOD extrahiert wurde. Die am stärksten angefachten RA-Responses treten im gleichen, niedrigen Frequenzbereich auf, wo auch die SPOD-Moden Low-Rank-Verhalten aufweisen. Ein Vergleich der räumlichen Moden-Formen von RA und SPOD zeigt äußerst gute Übereinstimmungen. Die zugehörigen Forcing-Moden sind lokal auf Regionen beschränkt in denen die größten Dichte-Gradienten auftreten und suggerieren, dass die nicht-homogene Dichte einen signifikanten Einfluss auf die Strömungsdynamik hat.

Aufgrund der Beobachtung eines sehr dominanten Mechanismus durch die Low-Mach-RA, wird die globale LSA motiviert. Das Spektrum der LSA zeigt gleich mehrere schwach gedämpfte Moden auf. Davon sind alle bis auf eine auf numerische Artefakte oder ein räumlich zu kurzes Rechengebiet zurückzuführen. Nachdem diese unphysikalische Moden ausgeschlossen werden, bleibt eine axialsymmetrische Mode erhalten. Diese führt die dominanten Moden der SPOD und RA auf eine Resonanz von stochastischem Forcings mit der schwach-gedämpften LSA-Mode zur $\frac{1}{4}ck$. Der sehr dominanten Dynamik der Strömung liegt eine globale, schwach gedämpfte Mode zugrunde. Eine adjungierte LSA identifiziert die Region größter Sensitivität gegenüber externer Anregung. Diese deckt sich mit der räumlichen Verteilung des optimalen Forcings der RA. Des weiteren ermittelt die strukturelle Sensitivität der Strömung eine kleine Region absoluter Instabilität nahe der Austrittskante zwischen Haupt- und Sekundärdüse, wo der Ursprung der globalen Mode ermittelt wird. Diese Ergebnisse, sowie die Verbindung zur RA, suggerieren, dass der mit der Flamme assoziierte Dichte-Abfall für die überaus dominante Dynamik im niederfrequenten Bereich verantwortlich ist.

Abstract

This thesis identifies and investigates coherent structures in incompressible, turbulent, non-reacting and reacting jet flows based on Large-Eddy Simulation (LES) data. While Spectral Proper Orthogonal Decomposition (SPOD) is applied to time-resolved snapshots to empirically decompose the flow fields into spatio-temporal coherent modes, global Resolvent Analysis (RA) based on the temporal mean fields finds the flow's response to optimal forcing. Global Linear Stability Analysis (LSA) is applied to the reacting jet flow to further investigate the driving mechanisms responsible for the coherent dynamics. The analysis of the non-reacting jet flow is based on the linearized incompressible Navier-Stokes equations (LNSE). The influence of the flame is taken into account by a non-uniform density-governing equation in the low mach limit, which serve as foundation for the RA and LSA of the reacting jet flow. All methods are applied within a bi-global framework presenting results from axisymmetric and helical analyses.

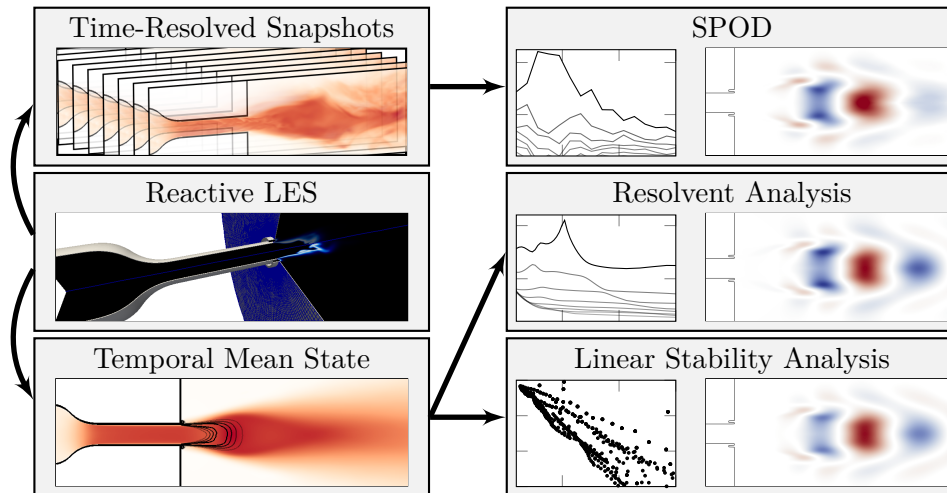
In the non-reacting jet flow, SPOD recovers the most energetic modes - low-rank behavior - by an axisymmetric analysis within the intermediate frequency regime, which are known as Kelvin-Helmholtz-type wavepackets. RA obtains the same flow dynamics and identifies these dynamics as amplified responses to harmonic optimal forcing within the same frequency regime. The optimal forcing displays the Orr-mechanism inside the boundary layer of the main nozzle. For the helical analysis, a similarly good agreement of SPOD- and RA-dynamics is obtained. Low-rank behavior is exhibited within the intermediate but also within the zero-approaching frequency regime. Both results from SPOD and from RA are compared with recently published literature and show a good agreement.

SPOD results of the reacting jet flow significantly differ from the results of the non-reacting jet flow. The most dominant modes, energy-wise, shift from the intermediate to the low-frequency regime. They exhibit a strikingly dominant low-rank behavior and incorporate up to 40% of the flow's turbulent, kinetic energy wrt. the axisymmetric structures. Similar to the non-reacting jet, the low-rank behavior weakens in the axisymmetric framework when zero frequencies are approached. Helical structures, instead, preserve their energy-dominance for very low frequencies. The overall flow dynamics resemble those obtained within the non-reacting configuration.

As intermediate step to applying the Low-Mach equations, first, the RA based on the non-reacting LNSE is applied to the mean fields obtained from the reactive LES. Although, this type of RA-approach is incapable of capturing the same dynamics as the SPOD, it presents the importance of taking the inhomogeneous density into account and motives the Low-Mach approach.

The Low-Mach-RA obtains the same dynamics as the SPOD does. Most amplified RA-responses occur in the same low-frequency regime as the most-energy incorporating structures do in the SPOD. The corresponding dynamics of the RA-responses are compared to the SPOD-modes and are in very good agreement. Corresponding forcing modes are spatially confined to regions of high density gradients and therefore, suggest the non-uniform density as driver of the significantly dominant dynamics.

Due to the Low-Mach-RA displaying a very dominant mechanism in a certain band of frequencies, global LSA is applied in order to investigate this behavior. The LSA-spectra present multiple weakly dampened modes, where all excepting one are linked to numerical artifacts and domain truncation. After excluding these modes, one mode remains in the axisymmetric analysis, and finally, explains the dominant modes seen both in SPOD and RA: They occur due to resonance of stochastic forcing with the damped LSA mode. An adjoint analysis displays the region most sensitive to external forcing which coincides spatially with the location of optimal RA-forcing. The system's structural sensitivity identifies a small pocket of absolute instability close to the nozzle's exit edge and localizes the origin of the global mode. These results and the link to the RA suggest the density drop due to the flame as driving cause behind the dominant dynamics.



Contents

1	Introduction	1
2	Theoretical Foundations	7
2.1	Linearized Equations	7
2.2	Resolvent Analysis	13
2.3	Linear Stability Analysis	16
2.4	Finite-Element Method	17
2.5	Spectral Proper Orthogonal Decomposition	18
3	Flow Configuration and Numerical Framework	21
3.1	Large Eddy Simulation	21
3.2	Mean Flows and Time-Resolved Snapshots	23
3.3	Spatial Discretization of the Linear Operators	24
3.4	Numerical Framework for Spectral Proper Orthogonal Decomposition	26
4	Results - Spectral Proper Orthogonal Decomposition	29
4.1	Non-Reacting Jet Flow	29
4.2	Reacting Jet Flow	31
5	Results - Linear Framework	35
5.1	Eddy-Viscosity Model Evaluation	35
5.2	Cold-Flow Resolvent Analysis of the Non-Reacting Jet Flow	38
5.3	Cold-Flow Resolvent Analysis of the Reacting Jet Flow	41
5.4	Low-Mach Resolvent Analysis of the Reacting Jet Flow	43
5.5	Linear Stability Analysis of the Reacting Jet Flow	47
6	Conclusion	51
	Bibliography	53

List of Figures

1.1	Model Energy Cascade:	2
1.2	Noise radiated by single components and total engine noise of an aircraft turbojet	3
3.1	Instantaneous snapshot of the flame	23
3.2	dimensionless LES- mean fields and snapshots	24
3.3	triangular discretization of the computational domain	25
4.1	m^0 -SPOD-results for the non-reacting jet flow	30
4.2	m^1 -SPOD-results for the non-reacting jet flow	31
4.3	m^0 -SPOD-results for the reacting jet flow	32
4.4	m^1 -SPOD-results for the reacting jet flow	33
5.1	Characteristic flow quantities within the Semeraro eddy-viscosity model	36
5.2	Characteristic flow quantities within the TKE eddy-viscosity model	37
5.3	Eddy-viscosity-model evaluation: comparison of SPOD-mode and RA-responses at $St = 0.66$	38
5.4	Comparison of m^0 -SPOD and -RA results for the non-reacting jet flow	39
5.5	Comparison of m^1 -SPOD and -RA results for the non-reacting jet flow	40
5.6	Optimal RA-forcing corresponding to the leading RA-responses presented in fig.5.4 and 5.5	41
5.7	Comparison of m^0 -SPOD of the reacting jet flow and Cold-Flow-RA results for the reacting jet flow	42
5.8	Optimal RA-forcing corresponding to the leading RA-responses presented in fig.5.7	43
5.9	Comparison of Low-Mach- m^0 -RA and SPOD results for the reacting jet flow	43
5.10	Comparison of Low-Mach- m^1 -RA and SPOD results for the reacting jet flow	44
5.11	Comparison of m^0 -and m^1 -SPOD-modes to RA-responses labeled as non-physical	45
5.12	Optimal Low-Mach-RA-forcing corresponding to the leading RA-responses presented in fig.5.9 and 5.10	46

5.13	Optimal Low-Mach-RA-forcing corresponding to forcing modes presented in fig.5.12(b,f)	47
5.14	Comparison of Low-Mach- m^0 -LSA and SPOD results for the reacting jet flow	48
5.15	Comparison of Low-Mach- m^1 -LSA and SPOD results for the reacting jet flow	49
5.16	Adjoint LSA-modes of the Low-Mach-LSA at $St = 0.103$ and structural sensitivity approximation	49

List of Tables

3.1	boundary conditions for the FE-discretized linear problem (RA & LSA); boundaries Γ_i as assigned in figure 3.3	26
-----	--	----

List of Abbreviations

BC Boundary Condition(s)
CFD Computation Fluid Dynamics
DMD Dynamics Mode Decomposition
FELiCs Finite-Element Linear Combustion Solver
FEM Finite-Element Method
KH Kelvin-Helmholtz
LES Large-Eddy Simulation
LHS Left Hand Side
LNSE Linear Navier-Stokes Equation
LSA Linear Stability Analysis
m⁰ Axisymmetric
m¹ Helical
PDE Partial Differential Equation
RA Resolvent Analysis
RANS Reynolds-Averaged Navier-Stokes
RHS Right Hand Side
SGS Sub-Grid-Scale
(S)POD (Spectral) Proper Orthogonal Decomposition
TFC Turbulent Flame Speed Model

List of Symbols

Latin

- C** two-point space-time correlation tensor
 c_v isochoric heat capacity
 c_p isobaric heat capacity
 D nozzle diameter
 f forcing
 G spatial filter function
 i imaginary unit
 k heat conductivity
 k turbulent kinetic energy
L linear operator
 \mathcal{L} non-linear operator
 l_m mixing length
 m azimuthal wavenumber
 p pressure
 q arbitrary transport quantity
q stacked vector of arbitrary transport quantities
 \mathcal{R} resolvent operator
 R_s specific gas constant
S cross-spectral density tensor
 t time
 T temperature T time period
 u velocity
 v FEM test function
W weighting matrix

Greek

- α FEM expansion coefficient
 γ adiabatic exponent

Γ boundary
 ε a small, real number
 θ azimuthal coordinate
 λ SPOD-eigenvalue
 Λ structural sensitivity
 μ dynamic viscosity
 μ RA-gain
 ν kinematic viscosity
 ρ density
 τ temporal delay
 φ FEM basis function
 ϕ optimal RA-forcing
 Φ viscous heating
 \mathcal{X} SPOD-eigenvector
 ψ optimal RA-response
 ω complex angular frequency
 Ω domain interior

Dimensionless Quantities

Pr Prandtl number
 Re Reynolds number
 St Strouhal number

Subscripts

eff effective
 max maximum
 min minimum
 r radial
 ref reference
 t turbulent
 x streamwise
 θ azimuthal

CHAPTER 1

Introduction

Turbulence not only is one of the most challenging research areas in fluid dynamics, but also in classical physics in general. Richard Feynman, Nobel prize winner in physics in 1965, states [3]

Finally, there is a physical problem that is common to many fields, that is very old, and that has not been solved. It is not the problem of finding new fundamental particles, but something left over from a long time ago - over a hundred years. Nobody in physics has really been able to analyze it mathematically satisfactorily in spite of its importance to the sister sciences. It is the analysis of circulating or turbulent fluids.

and called turbulence the 'most important unsolved problem of classical physics'. In fact, decades after Feynman's statement, the problem of turbulence still is unsolved and is part of the Millennium Prize Problem of finding a smooth solution to the Navier Stokes equations [4]. However, in addition to the 'importance to the sister sciences', the impact of turbulence on society in general is probably of the same order. Turbulent flows can be found in a vast field of industrial applications such as in transportation, power generation or in process engineering. Among many more, some of the effects of turbulence on the environment deal with the efficiency of transportation systems, such as cars and trains, with the noise emission of planes or the save operation of power generation system such as water turbines. And even though, there has not yet been found a fundamental solution the problem of turbulence, all these problems incorporate turbulent effects. In fact, engineers understand many of the most important phenomena connected to turbulence and managed to adapt designs and schemes to further improve the system. Many of these improvements rely on an important finding of turbulence research, the so-called energy cascade, which describes the transport of turbulent, kinetic energy from large to small scales, until the kinetic energy of motion dissipates due to viscosity. Figure 1.1 shows a schematic for this phenomena. It can be seen that structures of larger spatial wavenumber incorporate a higher energy amount than smaller structures. In fact, it is this large-scale, energy-dominating motion which is of such high importance for engineering applications. Within this region so-called coherent structures are mostly responsible for the phenomena

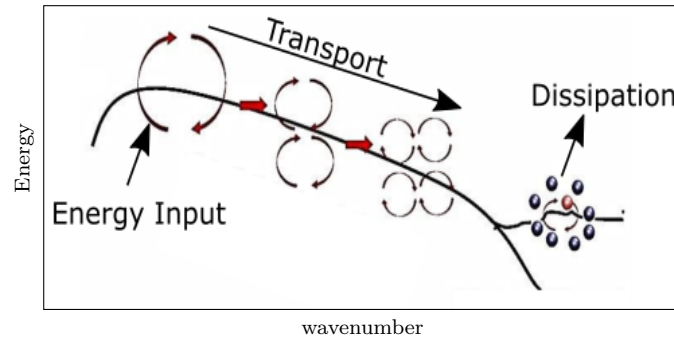


Figure 1.1: Model Energy Cascade: energy distribution and transport wrt. the wavenumber; extracted and modified from Khalaji [1]

mentioned above. In contrast to the stochastic fine-scale motion, these coherent structures follow a deterministic behavior, mostly influenced by boundary and initial conditions. Due to their importance, and due to their connection to the boundary conditions, it is crucial to identify such structures and investigate the underlying mechanism. In this context, the pioneering studies of Crow and Champagne [5] and Brown and Roshko [6] build the historical foundation for this field of research. The authors of both studies investigated turbulent shear flows experimentally and found such large-scale structures within their analysis. One study object was a turbulent jet flow, which is also the object of study within this thesis, where a non-reacting as well as a reacting configuration is investigated.

Although turbulent jet flows seem generic and trivial at first sight, they offer a great variety of effects as well as find their ways directly into industrial applications. One prominent application of a non-reacting jet is the flow exiting an aircraft engine to generate thrust. Within this example it is the coherent structures within the jet's shear layer which cause a major portion of the engine's noise radiation. As aircrafts are an important part of our all-day life, either in the field of cargo- or human transportation, the noise radiated by an aircraft engine has a major impact on the society in a variety of aspect. In fact, regulations to reduce aircraft noise are continuously tightened. Hence, the coherent structures are of special interest. To further lower the emitted noise, these structures have to be identified and the underlying mechanisms have to be investigated to find schemes which suppress the noise radiation.

Most often, however, turbulence does not occur as separated phenomenon in applications, rather than interacts directly with other physical phenomena, such as combustion process, i.e. chemical reactions. Due to a very strong mutual interaction of turbulence and combustion process, these system often exhibit a high complexity. The turbulent fluid motion impacts the chemical reaction within the flame, and hence, causes fluctuations within the combustion process. This, consequently, causes unsteady heat release, which again impacts

the flow's motion. It is this highly dynamical behavior which causes major challenges in industrial applications, such as in combustors of stationary gas turbines or of aircraft engines. However, the coherent structures play a crucial role for such systems as well. As they represent also the reacting flow's most energetic and large-scale structures, they are important for characteristics such as the mixing of fuel and oxidizer or the flame stability. Regarding the above example of noise emission within the field of aviation, turbulent combustion and the resulting combustion noise has a major impact on the engine's total noise emission. Due to recent progress in the field of jet noise and other disciplines such as fan noise, the portion of combustion noise on the total noise emission becomes even more important (fig. 1.2), motivating the research to understand the underlying mechanism and to develop methods to avoid these negative effects of turbulent combustion. Leylekian et al. [7] gives an overview on the progress in aircraft noise in general. Dowling and Mahmoudi [2] gives a review on combustion noise itself.

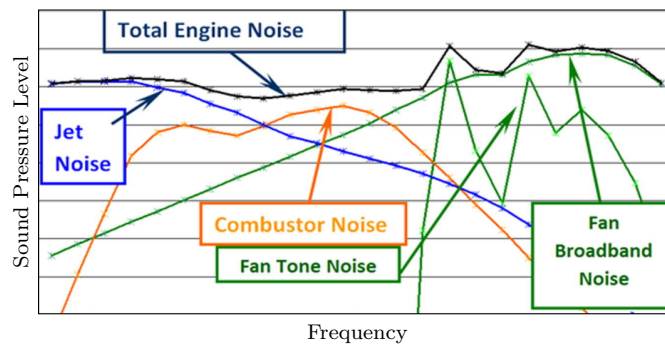


Figure 1.2: Noise radiated by single components and total engine noise of an aircraft turbojet; extracted and modified from Dowling and Mahmoudi [2]

The above examples show the importance of coherent structures in industrial applications. To investigate fluid flows in general, two major fields evolved during the last decades. Regardless of the exact field, they can be distinguished into experimental and numerical methods. However, they rather serve as data machinery, and can be considered as experiments in a wider sense. Within this study, data from a numerical experiment, a so-called Large-Eddy Simulation (LES) is analyzed. Nonetheless, it is the subsequent analysis methods which reveal the underlying principles, rather than (numerical) experiments themselves.

Many methods evolved to analyze the most important features of turbulence. Roughly, they can be split up into empirical methods and operator-based approaches. Generally, these techniques are referred to as modal decomposition or modal analysis methods. Both rely on data acquired by (numerical) experiments, and have different requirements on the data. However, both result in a decomposition of the flow into so-called modes of which some represent the most important features of the flow. A thorough overview of modern modal decomposition methods can be found within the reviews by Taira et al. [8] and Rowley and Dawson [9]

When referring to data-driven or empirical mode decomposition methods, usually, multiple samples of possibly several quantities of a flow field are required. Examples for empirical mode decomposition are the Fourier analysis, dynamic mode decomposition (DMD) or Proper Orthogonal Decomposition. Each of these methods is suited for different purposes. Fourier analysis decomposes the flow field fluctuations into monofrequent Fourier modes, DMD computes similar, monofrequent modes but also associates a growth (or decay) rate to each mode, and POD decomposes the flow field into orthogonal modes which capture as most as possible of the fluctuation energy with as few modes as possible. All of them present well-suited methods to extract coherent structures, however, each of them has a special field of application. Within this study the focus, regarding data-driven modal decomposition, lies on extracting the most dominant structures wrt. the energy, suggesting POD as most suitable. However, also a decomposition within the temporal domain is sought, suggesting the so-called spectral POD (SPOD) as most suitable candidate for the analysis carried out in this study.

In contrast to POD, SPOD not only decomposes the fluctuating flow field into space-coherent structures, but rather into spatio-temporal coherent modes. Despite this advantage, SPOD was less used than POD since, their introduction by Lumley [10]. Reasons therefore, concern the availability of time-resolving experimental measuring methods, such as particle image velocimetry, or the requirement of relatively long data series which result in prohibitively long time-integrations from a simulation point of view [11]. However, within the recent years the application of SPOD to fluid dynamics drastically increased and many different flow configurations have been analyzed. Among others, SPOD-analysis has been performed to extract the flow dynamics for turbulent pipe flows by Abreu et al. [12], for the flow over a NACA-airfoil by Abreu et al. [13] or for the wake of a vertical-axis wind turbine by Schmidt and Colonius [14]. Besides those, many studies have been performed wrt. turbulent non-reacting, subsonic, transonic and supersonic jets([15], [11], [16], [17]). However, to the author's best knowledge, only the SPOD-analysis of Shoji et al. [18] regarding a low-swirl jet flame is known in the field of reacting flows.

In the field of operator based modal analysis, also a variety of methods evolved during the last decades. Usually, these methods are based on some kind of governing equations. In contrast to conventional CFD-approaches, however, it is not the non-linear equations which are analyzed. In fact, the non-linear system usually has to be linearized before a modal analysis of the equations can be performed.

One of the most famous category of operator-based modal decomposition is the so-called linear stability analysis(LSA). Originally, this framework applied to laminar flows, where the governing differential equations are subject to a perturbation ansatz, where the quantities are perturbed around the system's solution. These perturbations are infinite small, and hence, justify the linearization, due to the fact that non-linear terms become very small. The solution of these problems give information whether the perturbations grow or decay wrt. time and space. However, it was shown that this approach also can be applied to turbulent flows. Instead of a perturbation ansatz, a triple decomposition([19]), the

decomposition into temporal mean, coherent fluctuations and stochastic fluctuations, is substituted into the governing equations, which are subsequently linearized around the mean flow and wrt. to the coherent fluctuations. This analysis aims on the evolution of coherent fluctuations growing or decaying wrt. time and space. In this approach, however, non-linear terms cannot be assumed to be very small since it is not infinite small perturbations which are considered but coherent fluctuations. However, it were Marasli et al. [20] and Mantič-Lugo et al. [21], who showed that the mean flow takes the non-linear interactions of coherent structures into account. As coherent structures grow within a flow they induce so-called coherent Reynolds stresses which modify the mean flow in such a way that it implicitly accounts for non-linearities.

Furthermore, there are certain sub-categories of LSA. Under the assumption of spatial homogeneity, it suffices to only analyze a slice or a profile of the flow at a certain location, yielding the local LSA. This ansatz was successively applied within a variety of studies([22], [23], [24], [25], [26]). However, the strong assumption of slowly diverging flow not always holds, or does not result in satisfying results. Global LSA overcomes this problem and studies the evolution of coherent structures in a global sense, either in three dimensions [27] [28] [29], often referred to as tri-global or under the assumption of homogeneity of one direction, referred to as bi-global [30] [25] [31] [32].

Concerning turbulent jets, LSA was an important tool to investigate the underlying mechanisms. Crighton and Gaster [33] applied local LSA to experimentally measured flow profiles of a turbulent jet and found that the initial shear-layer is convectively unstable. Similar observations were made by Cooper and Crighton [34] who found a weakly stable mode within the intermediate frequency regime. These observations display important dynamics turbulent jets which are known as KH-type wavepackets today. However, these analyses were performed under the assumption of weakly non-parallel flows. When studying an incompressible turbulent jet in a global framework, Garnaud et al. [35] found that there is no preferred mode globally. Hence, it can be concluded that such turbulent jets do only exhibit a local but not a global instability.

Similar to the application to non-reacting flows, global LSA often is used to analyze a reacting flow's stability such as by Paschereit et al. [36] or Paredes et al. [25]. However, many of these studies neglect any influence of the flame, as they only consider the linearized equations governing incompressible, non-reacting flow. In contrast, to that Kaiser [30] additionally derives a linear equation governing the non-uniform density due to the flame and applies bi-global LSA to an industrial combustor system. In fact, non-uniform density plays a crucial role for the stability of a flow and was investigated by Huerre and Monkewitz [37], Yu and Monkewitz [38] or Nichols et al. [39], by means of LSA.

Besides the LSA, a further method, the so-called resolvent analysis (RA), developed within the recent years and showed promising results wrt. analyzing coherent structures in turbulent flows. RA has its origins in control theory [8]. Concerning fluid dynamics, the RA roots within the forced linear Navier-Stokes operator, and was first exploited by Trefethen et al. [40]. When introducing a generic forcing to the linear equations, a linear mapping of that particular forcing onto a so-called response can be derived. The linear

transfer function in-between is the so-called resolvent operator, which usually is built wrt. to a turbulent mean flow. A singular-value-decomposed of the resolvent operator, then, gives information of the system's amplification characteristics. Regarding the bi-global RA many turbulent flows were analyzed. Monokrousos et al. [41] and Sipp and Marquet [42] used RA to investigate Tollmien-Schlichting waves within boundary layers. Kaiser et al. [43] investigates the swirling flow's response to external forcing. A backward facing step flow was analyzed by Beneddine et al. [44]. Regarding turbulent, non-reacting jets there is huge variety of studies. Among others ([15], [11], [45], [46]), Garnaud et al. [35] investigates the origin KH-type wavepackets in an incompressible jet and finds the RA-forcing to represent the Orr-mechanism within the boundary layer of the nozzle. Similar to Beneddine et al. [44], Beneddine et al. [47] reconstructs the turbulent field by projecting flow data measured by probes onto the resolvent modes. Extensive studies concerning non-axisymmetric perturbations were carried out by Nogueira et al. [16] and Pickering et al. [17].

However, to the author's best knowledge, the application to reacting flows is only covered by Kaiser et al. [43], where the authors not only analyze the RA-response to acoustic forcing for a non-reacting, but also for a reacting swirl flow, i.e. for a turbulent swirl flame.

As the above examples show the capabilities of empirical as well as operator-based methods in studying coherent structures and the underlying mechanisms in turbulent flows, this study aims to apply these methods to a turbulent jet flow in non-reacting and reacting configuration. To investigate the flow dynamics this study follows a certain strategy for both flow configurations that is non-reacting and reacting. First, the flow is analyzed by SPOD, giving first insights into the dynamics. Subsequently, the linear framework methods are validated wrt. SPOD-modes, and hence, allow to study the driving mechanism of the flow dynamics.

This thesis is structured as follows: This introduction is followed by the chapter outlining the theoretical foundations for the methods used (2). Then, the flow configuration, the LES and the numerical strategy followed within this thesis are presented (3). Subsequently, the results of the SPOD for both the non-reacting and reacting jet flow reveal the flow dynamics (4). Then, these results built the validation basis for the following RA-results for both flow configurations. Dynamics of the RA are compared to the SPOD and further analyzed, leading to the underlying mechanism (5), followed by the thesis conclusion (6). During the results sections, it occurs convenient to compare the results to findings from other studies. Especially for the non-reacting jet flow, many studies have been performed for both the SPOD and the linear framework. However, to the author's best knowledge, neither SPOD, nor RA have been studied within the reacting jet flow configuration except the applications which are mentioned above.

CHAPTER 2

Theoretical Foundations

The following chapter covers the theoretical foundations for this study. First, the linearized equations are derived for the Low-Mach and passive flame approach. The equations governing the non-reacting jet flow are incorporated within the Low-Mach equations and can be extracted. The linear equations serve as basis for the RA and LSA, which are outlined, subsequently. Then, the theoretical basis for Finite-Element Method (FEM) is covered. Finally, the SPOD-method is explained. This study covers a broad variety of analysis methods. A detailed study of each method goes far beyond the framework of this work. This chapter instead focuses on the most important aspects of each method. For further insights into the theoretical foundations the interested reader is referred to the literature mentioned within each section of this chapter. Within this thesis a quantity q or \mathbf{q} often is mentioned. It always represents an arbitrary quantity within the current context if not declared otherwise.

2.1 Linearized Equations

Non-Linear Governing Equations

A reacting flow is governed by transport equations for mass, momentum, energy and species mass fraction. These system often exhibit a high complexity and can take various forms (Poinsot and Veynante [48]). However, the goal of this study is to describe the hydrodynamics of coherent structures in a reacting flow, and not to exactly model the combustion process itself. Hence, the influence of different species being present is assumed to have a minor effect on the flow dynamics. Furthermore, the influence of the heat release due to the chemical reaction is neglected within the linear framework. Instead, a transport equation for the density is derived, accounting for the fluid's expansion due to the flame's heat release. With the above assumptions, the governing system reduces to transport

equations governing mass, momentum and internal energy ([30])

$$\begin{aligned} \partial_t \rho + \nabla \cdot \rho \mathbf{u} &= 0 \\ \rho (\partial_t \mathbf{u} + (\mathbf{u} \cdot \nabla) \mathbf{u}) &= -\nabla p + \nabla \cdot \left[\mu \left((\nabla + \nabla^T) \mathbf{u} - \frac{2}{3} \nabla \cdot \mathbf{u} \right) \right] \\ \rho (\partial_t (c_v T) + \mathbf{u} \nabla \cdot (c_v T)) &= -p \nabla \cdot \mathbf{u} + \nabla (k \nabla T) + \Phi \end{aligned} \quad (2.1)$$

To derive an equation governing the transport of density, the fluid is assumed as ideal gas with the following relations

$$p = \rho R_s T, \quad c_p - c_v = R_s, \quad \frac{c_p}{c_v} = \gamma, \quad \frac{R_s}{\gamma - 1} = c_v \quad (2.2)$$

which are substituted into the system 2.1. Under the assumptions of constant isochoric specific heat c_v , constant specific gas constant R_s and constant heat conductivity k , the gas properties can be pulled in front of the derivative operators. Additionally, the Low-Mach assumption (Poinsot and Veynante [48]) is applied, which further simplifies the governing system as follows. First, the viscous heating term Φ in eq. 2.1 is negligible. Second, the Low-Mach assumptions implies that density variations are decoupled from pressure fluctuations. Additionally, low Mach-number flames can be considered as constant pressure deflagration where the pressure equals the thermodynamic pressure $p = \rho R_s T$. Hence, the pressure can be pulled in front of the derivative operators. Taking the above assumptions into account and after some trivial operations, the density governing equation yields

$$\partial_t \rho + \mathbf{u} \cdot \nabla (\rho) = \rho (\gamma - 1) \nabla \cdot \mathbf{u} - \rho \frac{k}{c_v} \left(\frac{2}{\rho^3} \nabla \rho \cdot \nabla \rho - \frac{1}{\rho^2} \Delta \rho \right) \quad (2.3)$$

After identifying parts of the continuity equation in the LHS of the above equation and after multiplying by ρ^3 , the final density equation governing the non-uniform density is obtained.

$$\gamma \rho^3 \nabla \cdot \mathbf{u} = \frac{k}{c_v} (2 \nabla \rho \cdot \nabla \rho - \rho \Delta \rho) \quad (2.4)$$

This equation replaces the third equation in eq. 2.1.

For a better comparison of the results the equations are considered in dimensionless form. The nozzle exit diameter D and the streamwise exit velocity on the jet axis are chosen as characteristic length and velocity scale, such that the Reynolds number and Prandtl number yield

$$Re = \frac{\rho_{ref} u_{ref} D_{ref}}{\mu}, \quad Pr = \frac{c_p \mu \rho_{ref}}{k} \quad (2.5)$$

After scaling the equations with these characteristic quantities, finally, the following non-linear equations are obtained

$$\begin{aligned} \partial_t \rho + \nabla \cdot \rho \mathbf{u} &= 0 \\ \rho (\partial_t \mathbf{u} + (\mathbf{u} \cdot \nabla) \mathbf{u}) &= -\nabla p + \nabla \cdot \left(\frac{1}{Re} \left((\nabla + \nabla^T) \mathbf{u} - \frac{2}{3} \nabla \cdot \mathbf{u} \right) \right) \\ \rho^3 \nabla \cdot \mathbf{u} &= \frac{1}{Re Pr} (2 \nabla \rho \cdot \nabla \rho - \rho \Delta \rho) \end{aligned} \quad (2.6)$$

These equations govern mass and momentum transport and include an equation describing the inhomogeneous density due to a low Mach-number flame being present. Furthermore, they capture the non-reacting case. When a constant density is substituted, the third equation vanishes and the continuity equation yields the solenoidality condition making the dilatation term (the last term) in the momentum equation vanish.

Linearization

To describe the dynamics of coherent structures in a linear framework, the system 2.6 needs to be linearized around the mean flow. This study follows the procedure of Reynolds and Hussain [19] and their triple decomposition approach $\mathbf{q} = \overline{\mathbf{q}} + \tilde{\mathbf{q}} + \mathbf{q}'$. The overline, tilde and prime indicate the temporal mean, the coherent fluctuations and the stochastic fluctuations, respectively. The temporal mean is obtained as $T^{-1} \int_0^T q dt$, where the coherent fluctuations are $\tilde{q} = \langle q \rangle - \bar{q}$, and the $\langle \cdot \rangle$ indicates the phase average:

$$\langle q(t) \rangle = \lim_{N \rightarrow \infty} \frac{1}{N} \sum_0^{N-1} q(t + n\tau) \quad (2.7)$$

Then, the triple decomposition is substituted into the governing equations, which are subsequently phase averaged. After subtracting the temporal mean and some other repeating operations, one arrives at the linearized Navier-Stokes equations (LNSE). Since the linearization procedure is similar for all three equations in principle, this derivation will not show each step for each equation. Instead, the linearization of the continuity equation is presented as illustrative example. However, some specific terms arising in the other equations and their treatment will be presented as well. For a rigorous derivation the reader is referred to Kaiser [30].

First, the triple decomposition is substituted into the continuity equation (eq. 2.6) and a phase average is applied, resulting in:

$$\begin{aligned} 0 = \langle \partial_t \bar{\rho} + \nabla \cdot (\bar{\rho} \bar{\mathbf{u}}) + (\partial_t \tilde{\rho} + \nabla \cdot (\tilde{\rho} \tilde{\mathbf{u}} + \bar{\rho} \tilde{\mathbf{u}})) + (\partial_t \rho' + \nabla \cdot (\bar{\rho} \mathbf{u}' + \rho' \bar{\mathbf{u}})) \rangle \\ + \langle (\nabla \cdot (\tilde{\rho} \mathbf{u}' + \rho' \tilde{\mathbf{u}})) + \nabla \cdot \tilde{\rho} \tilde{\mathbf{u}} + \nabla \cdot \rho' \mathbf{u}' \rangle \end{aligned} \quad (2.8)$$

By using the linearity of the phase average, it can be pulled into each term of the above equation, where then, the following identities hold:

$$\begin{aligned} \langle \bar{q} \rangle &= \bar{q} & \langle \bar{q}\bar{q} \rangle &= \overline{q\bar{q}} & \langle \bar{q}\tilde{q} \rangle &= \bar{q}\tilde{q} \\ \langle \tilde{q} \rangle &= \tilde{q} & \langle \tilde{q}\tilde{q} \rangle &\neq 0 & \langle \bar{q}q' \rangle &= 0 \\ \langle q' \rangle &= 0 & \langle q'q' \rangle &\neq 0 & \langle \tilde{q}q' \rangle &= 0 \end{aligned} \quad (2.9)$$

Applying these identities, and taking into account that $\partial_t \overline{(\cdot)} = 0$, eq. 2.8 reduces to

$$\nabla \langle \bar{\rho}\bar{\mathbf{u}} \rangle + [\partial_t \tilde{\rho} + \nabla(\bar{\rho}\tilde{\mathbf{u}} + \tilde{\rho}\bar{\mathbf{u}})] + \nabla \langle \tilde{\rho}\tilde{\mathbf{u}} \rangle + \nabla \langle \rho'\mathbf{u}' \rangle = 0 \quad (2.10)$$

Subsequently, eq. 2.10 is temporally averaged where the following identities are obtained

$$\overline{\langle \tilde{q} \rangle} = 0 \quad \overline{\langle \bar{q}\bar{q} \rangle} = 0 \quad \overline{\langle \tilde{q}\tilde{q} \rangle} = \overline{\tilde{q}\tilde{q}} \neq 0 \quad \overline{\langle q'q' \rangle} = \overline{q'q'} \neq 0 \quad (2.11)$$

such that the temporal mean of the phase averaged equation results in

$$\nabla(\overline{\rho\mathbf{u}}) + \nabla(\overline{\tilde{\rho}\tilde{\mathbf{u}}}) + \nabla(\overline{\rho'\mathbf{u}'}) \quad (2.12)$$

After subtracting eq. 2.12 from 2.10 the following equation is obtained:

$$[\partial_t \tilde{\rho} + \nabla(\tilde{\rho}\tilde{\mathbf{u}}) + \nabla(\tilde{\rho}\bar{\mathbf{u}})] + \nabla[\langle \tilde{\rho}\tilde{\mathbf{u}} \rangle - \overline{\tilde{\rho}\tilde{\mathbf{u}}}] + \nabla[\langle \rho'\mathbf{u}' \rangle - \overline{\rho'\mathbf{u}'}] = 0 \quad (2.13)$$

Where the term inside the first bracket is linear wrt. the coherent fluctuations $\tilde{\mathbf{q}}$, the term inside the second bracket is quadratic. In addition to this, terms of quadratic order wrt. to stochastic fluctuations \mathbf{q}' arise. Terms of this structure, i.e. displaying a non-linear interaction of density and velocity, are observed for all equations in 2.6 when following the above procedure. They occur due to the non-uniform density taken into account. In fact, to avoid such terms, one introduces a density-weighted Favre-average in conventional CFD-methods, e.g. when deriving the so-called Reynolds-Averaged-Navier-Stokes (RANS) equations [49]. However, this method does not yield a success in the case of linearization wrt. a phase average and remains an open problem [30]. Hence, all terms which display a non-linear interaction between density and velocity are neglected in all equations governing the linear framework within this thesis. Then, the linear continuity equation yields

$$\partial_t \tilde{\rho} + \nabla(\tilde{\rho}\tilde{\mathbf{u}}) + \nabla(\tilde{\rho}\bar{\mathbf{u}}) = 0 \quad (2.14)$$

For the remaining equations, the same procedure as outlined above is followed. In addition to the non-linear density-velocity interaction, also non-linear velocity-velocity interactions wrt. stochastic, as well as wrt. coherent fluctuations are obtained in the momentum equations. They arise due to the convective term and take the form

$$(\mathbf{u} \cdot \nabla)\mathbf{u} \rightarrow \underbrace{\langle \tilde{\mathbf{u}}\nabla\tilde{\mathbf{u}} \rangle - \overline{\tilde{\mathbf{u}}\nabla\tilde{\mathbf{u}}}}_{T_1} + \underbrace{\langle \mathbf{u}'\nabla\mathbf{u}' \rangle - \overline{\mathbf{u}'\nabla\mathbf{u}'}}_{T_2} \quad (2.15)$$

In contrast to the non-linear density-velocity interactions identified above, the velocity-velocity interactions are not neglected and will be investigated in the following. First, the term T_2 is considered which is rearranged using the product rule:

$$\langle \mathbf{u}' \nabla \mathbf{u}' \rangle - \overline{\mathbf{u}' \nabla \mathbf{u}'} = \frac{1}{2} \nabla \cdot \left(\langle \mathbf{u}' \mathbf{u}' \rangle - \overline{\mathbf{u}' \mathbf{u}'} \right) \quad (2.16)$$

In contrast to the density-velocity interaction, velocity-velocity interactions wrt. the stochastic fluctuations cannot be assumed as negligible [19]) and require modeling. In fact, similar terms arise in the RANS equations in CFD, the so-called Reynolds-stresses, when the momentum equations are Reynolds-decomposed. In conventional CFD, usually, a well-known model approach, the Boussinesq approximation, is used to model these terms. The Boussinesq approximation states that this term has an additional diffusion like influence on the transport quantities [49]. It is based on the more general gradient-diffusion hypothesis and relates the Reynolds stresses proportionally to the mean strain rate via a constant, the so-called turbulent viscosity or eddy-viscosity. This approach also is used when modeling the non-linear stochastic interactions arising in the linear framework. Within this thesis the same approach of Rukes et al. [31] is followed. However, it is adapted to the compressible Boussinesq hypothesis to suit a non-solenoidal flow.

$$\begin{aligned} \langle \mathbf{u}' \mathbf{u}' \rangle &= \frac{2}{3} \langle k \rangle \mathbf{I} - 2\nu_t^e \left(\nabla(\cdot) + \nabla^T(\cdot) - \frac{2}{3} \nabla \cdot (\cdot) \right) \langle \mathbf{u} \rangle \\ \overline{\mathbf{u}' \mathbf{u}'} &= \frac{2}{3} \overline{k} \mathbf{I} - 2\nu_t^t \left(\nabla(\cdot) + \nabla^T(\cdot) - \frac{2}{3} \nabla \cdot (\cdot) \right) \overline{\mathbf{u}} \end{aligned} \quad (2.17)$$

These equations relate the Reynolds-stress-like terms in eq. 2.16 to the turbulent kinetic energy k and the strain rates. The so-called eddy-viscosity acts as diffusivity-constant between stress and strain. For the approximation for the phase averaged stresses it is the turbulent viscosity ν_t^e , for the temporally averaged stresses it is ν_t^t . However, Viola et al. [24] shows that these terms are equal for the incompressible Boussinesq approximation, i.e. $\nu_t = \nu_t^t = \nu_t^e$. The same statement also holds for the compressible Boussinesq approximations. Furthermore, it is assumed that the phase-averaged and temporally averaged quantities differ wrt. their fine-scale structure but not wrt. their energy [24]. Hence, phase averaged kinetic energy equals temporally averaged energy. Finally, by taking into account that $\tilde{\mathbf{u}} = \langle \mathbf{u} \rangle - \overline{\mathbf{u}}$, T_2 is modeled as

$$\langle \mathbf{u}' \nabla \mathbf{u}' \rangle - \overline{\mathbf{u}' \nabla \mathbf{u}'} = \nabla \cdot \left[\nu_t \left(\nabla(\cdot) + \nabla^T(\cdot) - \frac{2}{3} \nabla \cdot (\cdot) \right) \tilde{\mathbf{u}} \right] \quad (2.18)$$

When following the procedure outline above and substituting eq. 2.18 into the momentum

equation, finally, the following set of equations is obtained:

$$\begin{aligned} \partial_t \tilde{\rho} + \bar{\mathbf{u}} \cdot \nabla \tilde{\rho} + \tilde{\mathbf{u}} \cdot \nabla \bar{\rho} + \tilde{\rho} \nabla \cdot \bar{\mathbf{u}} + \bar{\rho} \nabla \cdot \tilde{\mathbf{u}} &= 0 \\ \bar{\rho} (\partial_t \tilde{\mathbf{u}} + \tilde{\mathbf{u}} \cdot \nabla \bar{\mathbf{u}} + \bar{\mathbf{u}} \cdot \nabla \tilde{\mathbf{u}}) + \tilde{\rho} (\bar{\mathbf{u}} \cdot \nabla \bar{\mathbf{u}}) &= -\nabla \tilde{p} + \nabla \cdot \left[Re_{eff}^{-1} \left((\nabla + \nabla^T) \tilde{\mathbf{u}} - \frac{2}{3} \nabla \cdot \tilde{\mathbf{u}} \right) \right] + T_1 \\ \bar{\rho}^3 \nabla \cdot \tilde{\mathbf{u}} + 3\bar{\rho}^2 \tilde{\rho} \nabla \cdot \bar{\mathbf{u}} + (Re Pr)^{-1} (\bar{\rho} \Delta \tilde{\rho} + \tilde{\rho} \Delta \bar{\rho} - 4 \nabla \tilde{\rho} \nabla \bar{\rho}) &= 0 \end{aligned} \quad (2.19)$$

In fact, due to the term T_1 these equations are not completely linear wrt. coherent fluctuations. However, the treatment of term T_1 depends on the upcoming solution method, at least on a phenomenological level, and will be subject to the upcoming sections concerning the RA and LSA. Furthermore, it is noted, that the effective Reynolds number $Re_{eff} = \frac{\bar{u}_{ref} \bar{D}_{ref} \rho_{ref}}{\mu + \mu_t}$ includes molecular and turbulent viscosity.

In case of a uniform density flow the temporal mean density field is spatially constant and no density fluctuations occur. Hence, the third equation vanishes, continuity reduces to the solenoidality condition, which subsequently alters the momentum equations. Concludingly, the linear, non-reacting flow governing equations yield

$$\begin{aligned} \nabla \cdot \tilde{\mathbf{u}} &= 0 \\ \partial_t \tilde{\mathbf{u}} + \tilde{\mathbf{u}} \cdot \nabla \bar{\mathbf{u}} + \bar{\mathbf{u}} \cdot \nabla \tilde{\mathbf{u}} &= -\nabla \tilde{p} + \nabla \cdot Re_{tot}^{-1} (\nabla + \nabla^T) \tilde{\mathbf{u}} + T_1 \end{aligned} \quad (2.20)$$

Eddy-Viscosity Models

The Boussinesq approximation and the corresponding modeling of the turbulent viscosity is a well-known concept in conventional CFD when computing the RANS equations. However, the application of such a model has also become very common in LSA and RA (e.g. [24], [31], [46], [17], [50]). However, there has not evolved a favorable model for the eddy-viscosity. In the following, four different models are presented which are analyzed wrt. to the RA for the non-reacting jet flow. The results of this analysis are evaluated in section 5.1.

The first model, which, in the following, is referred to as ν^0 -model, completely neglects the turbulent viscosity and simply sets the effective Reynolds number to $Re = \frac{u_{ref} \bar{D}_{ref}}{\nu_{mol}}$ with $\nu_t = 0$. This approach implies that the non-linear interaction of stochastic fluctuations (T_2) is neglected.

The next model, introduces an artificial, spatially constant turbulent viscosity such that $\nu_t = m \nu_{mol}$, where $m \in \mathbb{R}$. The from her on labeled ν^m -model replaces the turbulent viscosity with a multiple of the molecular viscosity.

Where the first and second model are rather simple, the third and fourth are more sophisticated and both take the mean velocity as well as quantities related to the background turbulence into account. The third model, has its roots within the Boussinesq approximation itself. Assuming the Reynolds-stress tensor is completely known, one would be able to compute the turbulent viscosity directly via the Bousinnesq approximation. Nonetheless, this would result in six independent turbulent viscosities. There have been applications of this method, for instance Kaiser et al. [43], Rukes et al. [31] or Paredes et al. [25]

used a least square ansatz to reduce the multiple viscosities to one. However, expecting the x-r-component of the Reynolds-stresses to have a leading influence on the turbulent viscosity, Semeraro et al. [50] proposed a rather simpler approach, from now on referred to as Semeraro-model:

$$\nu_t = \frac{-\overline{u'_x u'_r}}{\partial_r \overline{u_x}} + \varepsilon \quad (2.21)$$

yielding a reduced Boussinesq ansatz, where ε is chosen as 10^{-4} to avoid a singularity when the derivative in the denominator vanishes.

Fourth, the model, which from now on is referred to as TKE-model, is presented. This model is based on the mixing length hypothesis proposed by Prandtl in 1925 $\nu_t = l_m u^*$ [49], which assumes the turbulent viscosity to scale proportionally with a characteristic length l_m as well as with a characteristic velocity u^* . In fact, this model often is applied in wall bounded flows in conventional CFD, and is based on the idea of turbulence having similar effects as the stochastic motion of molecules causing the molecular viscosity. However, instead of choosing a strain- based approximation for the characteristic velocity, Kolmogorov(1942) and Prandtl(1945) independently suggested to use a turbulent kinetic energy-related measure[49], such as $u^* = c\sqrt{k}$, with k as the turbulent kinetic energy and c as scaling constant, leaving the characteristic length scale up for discussion. Recently, Pickering et al. [46] performed RA including this mixing length model and achieved good results with it. This thesis, however, uses a different method to determine the streamwise varying length scale which is adapts a method from the field of combustion, i.e. for determining the flame thickness [48]. Similarly, the length scale is determined here, such as

$$l_m(x^*) = \frac{\overline{u_x}(x = x^*, r = 0) - \min(\overline{u_x}(x = x^*, r))}{\max(|\partial_r \overline{u_x}|_{x=x^*})} \quad (2.22)$$

where x^* is an arbitrary, but fixed streamwise position. Finally, the TKE-model results in

$$\nu_t = c l_m \sqrt{k} \quad (2.23)$$

where the scaling constant is chosen as $c = 0.05$.

2.2 Resolvent Analysis

In section 2.1 it is seen that a term of quadratic order wrt. coherent velocity fluctuations (T_1 in eq. 2.20 and 2.19) arises when the momentum equations are linearized. To finally solve the linear system with the RA, this term needs further attention. Within this thesis the term T_1 is substituted by a linear forcing term $\tilde{\mathbf{f}}_u$ acting as a momentum source within the linear momentum equations, finally, resulting in fully linear equations. Subsequently, a harmonic ansatz $\tilde{\mathbf{q}} := \hat{\mathbf{q}} \exp(i\omega t)$ for all coherent fluctuation quantities is substituted into these equations and results in the linear system

$$i\omega \mathbf{B} \hat{\mathbf{q}}(\omega) = \mathbf{L} \hat{\mathbf{q}}(\omega) + \hat{\mathbf{f}}(\omega) \quad (2.24)$$

where

$$\mathbf{B} = \begin{bmatrix} 0 & 1 & 0 \\ \bar{\rho} & 0 & 0 \\ 0 & 0 & 0 \end{bmatrix} \quad (2.25)$$

and

$$\mathbf{L} = \begin{bmatrix} \bar{\rho}\nabla(\cdot) + (\cdot)\nabla\bar{\rho} & \bar{\mathbf{u}} \cdot \nabla(\cdot) + (\cdot)\nabla \cdot \bar{\mathbf{u}} & 0 \\ (\cdot)\bar{\rho} \cdot \nabla\bar{\mathbf{u}} + \bar{\rho}\bar{\mathbf{u}} \cdot \nabla(\cdot) & (\cdot)\bar{\mathbf{u}} \cdot \nabla\bar{\mathbf{u}} & \nabla(\cdot) \\ -\nabla \cdot \left[Re_{eff}^{-1} \left((\nabla + \nabla^T)(\cdot) - \frac{2}{3}\nabla \cdot (\cdot) \right) \right] & & \\ \bar{\rho}^3 \nabla \cdot (\cdot) & (\cdot)3\bar{\rho}^2 \nabla \cdot \bar{\mathbf{u}} + (Re_{eff} Pr)^{-1} [\bar{\rho}\Delta(\cdot) + (\cdot)\Delta\bar{\rho} - 4\nabla\bar{\rho}\nabla(\cdot)] & 0 \end{bmatrix} \quad (2.26)$$

and $\hat{\mathbf{q}} = [\hat{\mathbf{u}} \hat{\rho} \hat{p}]^T$ and $\hat{\mathbf{f}} = [\hat{f}_u \ 0 \ 0]^T$. Then, the resolvent operator is introduced as $\mathcal{R}(\omega) = (i\omega\mathbf{B} - \mathbf{L})^{-1}$. Subsequently, the system identifies as linear mapping of the harmonic forcing onto the so-called harmonic response via the resolvent operator.

$$\hat{\mathbf{q}}(\omega) = \mathcal{R}(\omega)\hat{\mathbf{f}}(\omega) \quad (2.27)$$

In fact, this system is derived in many studies where the above replacing of the non-linear term T_1 by a forcing term $\hat{\mathbf{f}}$ is often pronounced by the authors. Beneddine et al. [44], for instance, directly define a turbulent forcing term $\mathbf{f} = T_1$. Similarly, McKeon and Sharma [51] define the forcing term and state that non-linearity is preserved by this treatment. Garnaud et al. [35], instead, introduces the forcing term as external forcing without any ambition to preserving non-linearity characteristics. In fact, as all the authors treat their equations with a similar harmonic ansatz as above, all of them imply a linear treatment of the forcing term. In the end, this discussion rather takes place on a phenomenological level. However, it is stated here, that the term T_1 is modeled by a generic, linear and coherent fluctuating momentum source $\hat{\mathbf{f}}$, which does not preserve any non-linearity. Further investigating the above system, a gain is defined as

$$\mu^2(\omega) = \frac{\int_{\Omega} \hat{\mathbf{q}}^* \mathbf{W} \hat{\mathbf{q}} d\Omega}{\int_{\Omega} \hat{\mathbf{f}}^* \mathbf{W} \hat{\mathbf{f}} d\Omega} \quad (2.28)$$

where \mathbf{W} is an appropriate weighting matrix and the *-superscript denotes the complex-conjugate. Throughout this thesis, the weighting matrix for the resolvent analysis is defined as $\mathbf{W}(\mathbf{x}) = \text{diag}(\bar{\rho}, 0, 0)$ and accounts for the inhomogeneous density field. It also can be seen that only fluctuations wrt. the velocity are accounted for. However, neither the harmonic forcing nor the harmonic response are known a priori. To find a solution to the above problem, it can be demanded to find a harmonic forcing $\hat{\phi}(\omega)$ which maximizes

the gain resulting in the maximization problem

$$\max_{\hat{\phi}} \mu^2(\omega) = \max_{\hat{\phi}} \left(\frac{\int_{\Omega} \hat{\psi}^* \mathbf{W} \hat{\psi} d\Omega}{\int_{\Omega} \hat{\phi}^* \mathbf{W} \hat{\phi} d\Omega} \right) \quad (2.29)$$

The optimal harmonic forcing $\hat{\phi}$ similarly is mapped to a optimal harmonic response $\hat{\psi}$ via the resolvent operator with $\hat{\psi}(\omega) = \mathcal{R}(\omega)\hat{\phi}(\omega)$.

To find a solution to the optimization problem stated in eq. 2.29 an arbitrary discretization of the resolvent operator can be applied. Later, in section 3.3, the discretization strategy is outlined in detail. However, assuming a discretized problem for now, the optimization problem yields

$$\max_{\underline{\hat{\phi}}} \mu^2(\omega) = \max_{\underline{\hat{\phi}}} \left(\frac{\|\underline{\hat{\psi}}\|_{\bar{\rho}}^2}{\|\underline{\hat{\phi}}\|_{\bar{\rho}}^2} \right) \quad (2.30)$$

where the underline indicates spatially discretized quantities and $\|(\cdot)\|_{\bar{\rho}}^2 = \bar{\rho} \|(\cdot)\|_2^2$ is the squared and density-weighted euclidian norm resulting from the discretization of the inner product in eq. 2.29. Additionally, the linear mapping of discretized forcing onto discretized response via the discretized resolvent operator $R(\omega)$, i.e. the discretization of eq. 2.27 can be substituted into eq. 2.30 resulting in

$$\max_{\underline{\hat{\phi}}} \mu^2(\omega) = \max_{\underline{\hat{\phi}}} \left(\frac{\|R(\omega)\underline{\hat{\phi}}\|_{\bar{\rho}}^2}{\|\underline{\hat{\phi}}\|_{\bar{\rho}}^2} \right) \quad (2.31)$$

Following Garnaud et al. [35], this problem can be decomposed and results in an eigenvalue problem

$$\mathbf{A}(\omega)\hat{\phi}(\omega) = \lambda(\omega)\hat{\phi}(\omega) \quad (2.32)$$

where the matrix $\mathbf{A}(\omega)$ incorporates the discretized resolvent operator, and some other matrices resulting from the decomposition of 2.31.

The eigenvalue problem formulated in eq. 2.32 can be solved for arbitrary frequencies ω and results in a set of RA-modes, which include N_{dim} eigenvectors representing the forcing and N_{dim} eigenvalues corresponding to the optimal gain. N_{dim} is the problems size and equals the size of the discrete resolvent operator. Furthermore, the forcing modes are pairwise orthogonal and can be mapped to a corresponding optimal response mode via the resolvent operator. Hence, the results obtained from the RA within this framework finds harmonic forcing and response modes which are optimal wrt. a amplification measure. This measure, i.e. the gain is said to exhibit low-rank behavior, when the leading mode's gain significantly separates magnitude-wise from the remaining gains. Such a behavior indicates that one forcing results in a significantly stronger amplified response than other forcings.

2.3 Linear Stability Analysis

In contrast to RA, LSA solves the linearized equations for coherent fluctuations directly. As in the above section, the term T_1 in eq. 2.20 and 2.19 requires further treatment to obtain a linear system. In terms of LSA this term is neglected, e.g. Rukes et al. [31]. This can be justified by findings of Marasli et al. [20], who found that non-linear interaction of coherent perturbations modify the mean flow. Hence, the LSA based on the turbulent mean flow accounts for term T_1 .

Then, the resulting linear system, can be solved directly. Therefore, a harmonic ansatz is chosen such as $\hat{\mathbf{q}} = \tilde{\mathbf{q}} \exp(-i\omega t)$. Hence, the linear system reduces to

$$i\omega \mathbf{B} \hat{\mathbf{q}}(\omega) = \mathbf{L} \hat{\mathbf{q}}(\omega) \quad (2.33)$$

posing a complex eigenvalue problem, where the operators \mathbf{L} and \mathbf{B} are the same as in section 2.2. $\hat{\mathbf{q}}$ incorporates the stacked solution quantities again. This system describes how harmonic perturbations evolve wrt. to the mean flow. Furthermore, an adjoint problem can be derived. Following Gianetti and Luchini [52], every direct eigenvalue problem has an adjoint counterpart. The adjoint problem reads

$$(i\omega)^\dagger \hat{\mathbf{q}}^\dagger(\omega) \mathbf{B} = \hat{\mathbf{q}}^\dagger(\omega) \mathbf{L} \quad (2.34)$$

where the \dagger -superscript indicates the adjoint eigenvalue and eigenvector.

Since the adjoint problem's solutions indicate the effect of the initial conditions on the solution of the direct problem, they are at least of same interest as the direct solutions themselves. In fact they display the system's receptivity against external forcing. However, to further investigate the instability the so-called wavemaker, i.e. the location where the strongest feedback occurs, is introduced and which can be identified as origin of the instability. Gianetti and Luchini [52] identify this location where

$$\Lambda(\mathbf{x}) = \frac{\|\hat{\mathbf{q}}^\dagger\| \|\hat{\mathbf{q}}\|}{\int_{\Gamma} \hat{\mathbf{q}}^\dagger \hat{\mathbf{q}} dS} \quad (2.35)$$

becomes large.

After discretizing the above direct 2.33 and adjoint problems 2.34, they can be numerically eigen decomposed. The solution of the direct eigenvalue problem gives so-called direct LSA-modes, incorporating the eigenvalue $\omega \in \mathbb{C}$, where $\text{Re}\{\omega\}$ is the harmonic frequency and $\text{Im}\{\omega\}$ the growth rate, and the spatial direct mode $\hat{\mathbf{q}} \in \mathbb{C}$. Similar holds for the solution of the adjoint eigenvalue problem, where the eigenvalue represents a measure for the receptivity to harmonic perturbations ($\text{Im}\{\omega^\dagger\}$) and the adjoint spatial mode $\hat{\mathbf{q}}^\dagger$ localizes regions of high receptivity.

2.4 Finite-Element Method

In the sections 2.2 and 2.3 systems of linear partial differential equations (PDES) are derived. To solve these systems they require a spatial discretization, which can be achieved by a variety of methods. Many schemes which use structured grids such as the Finite-Difference method (FDM), could be used to discretize the problem. However, methods based on structured grids often lack flexibility regarding the adaptivity of spatial resolution as well as the ability of capturing complex geometries. In contrast to methods based on structured grids, another famous approach, the Finite-Element method (FEM) can be applied to unstructured grids, enabling an adaptive resolution as well the mapping of complex geometries. In fact, these advantages over the structured grid methods, result in a large variety of applications of the FEM to various physical problems, e.g. solid and fracture mechanics, electromagnetics or fluid dynamics. Also the application to the discretization of the linearized Navier-Stokes equations often is found in the literature ([30] [43]). Due to the advantages mentioned, the FEM is also employed in this study, where the theoretical foundations of this methods are outlined on the example of the LSA-governing system in the following. This section refers mostly to Becker et al. [53]. For further insights into the method, the interested reader is referred this literature.

The linear system in eq. 2.27 also can be referred to as strong formulation:

$$\begin{cases} i\omega \mathbf{B}\hat{\mathbf{q}} = \mathbf{L}\hat{\mathbf{q}} \in \Omega \\ \mathbf{BC} \text{ on } \Gamma \end{cases} \quad (2.36)$$

where Ω indicates the inner of the domain and Γ is the boundary, on which certain boundary conditions BC hold.

The objective of the FEM is to approximate the solution of the system, i.e. $\hat{\mathbf{q}}$, as a superposition of simpler functions. As it can be seen from the equations in eq. 2.19 and eq. 2.20, the solution has to be continuously differentiable twice at least. This condition restricts the functions available, hence the formulation 'strong'. To lower the requirements on the solution and to allow the solutions to be out of a larger function space, first, the strong formulation is transferred to the weak formulation. Therefore, a set of so-called test functions $\mathbf{v} = [v_1, \dots, v_5]^T$, where $v_j \in H^1$ is multiplied onto the strong form in eq. 2.36. H^1 is the function space for all functions with existing first derivative and squared integral. After integrating this equation over the whole domain Ω , a scalar, integral equation is obtained

$$\int_{\Omega} \mathbf{v}^T \mathbf{L}\hat{\mathbf{q}} d\Omega = i\omega \int_{\Omega} \mathbf{v}^T \mathbf{B}\hat{\mathbf{q}} d\Omega \quad (2.37)$$

However, this form still requires the solutions to be continuously differentiable twice due to the second derivatives occurring within the diffusion terms. To decrease the requirements regarding differentiability, integration by parts, i.e. Greens first identity, is applied to these terms. For an arbitrary function $w \in \mathbb{C}$ and an arbitrary constant c this identity

holds:

$$\int_{\Omega} v_j \nabla \cdot (c \nabla w) d\Omega = \int_{\Gamma} v_j (c \nabla w) \cdot \mathbf{n} d\Gamma - \int_{\Omega} c \nabla v_j \cdot \nabla w d\Omega \quad (2.38)$$

where \mathbf{n} is the normal vector wrt. to the boundary Γ . Applying this scheme to all higher derivative terms in eq. 2.37 results in the weak formulation, where the solutions, the so called-trial functions, are now allowed from a larger function space, in this case from the same as the test functions are from. Since this function space is linear, functions inside this space can be expressed as linear combination of the basis functions $(\varphi_1(\mathbf{x}), \varphi_2(\mathbf{x}), \varphi_3(\mathbf{x}), \dots)$ of this space, resulting in

$$\hat{q} = \sum_{k=1}^{\infty} \alpha_k \varphi_k(\mathbf{x}) \quad (2.39)$$

a linear expansion of the solution, where α_k is a coefficient. However, test and trial space are of infinite dimension which needs to be reduced. One prominent way to do so is Galerkin's dimension reduction. Instead of considering test and trial spaces with infinite dimension, solutions on finite dimensional subspaces are sought. Test and trial space include a variety of allowed functions and hence, there a many choices. Within this work, two-dimensional domains are considered which are subdivided into triangular sub domains. Then, the test space can be reduced to the space of piecewise linear polynomial functions living on the nodal points of each triangular element, resulting in the so-called and name giving finite elements. By this choice the dimension of the subspace drastically is reduced compared to the infinite dimensional space and yields a finite dimensional subspace, finally, resulting in a finite, linear expansion of the solution

$$\hat{q}_N = \sum_{k=1}^N \alpha_k \varphi_k(\mathbf{x}) \quad (2.40)$$

where the test function $\varphi_k(\mathbf{x})$ now is known as the prior choice of a piecewise linear polynomial living on the nodes of each elements. This leads to a linear expansion of the approximate solution u_N where N is the amount of triangular elements. Subsequently, this ansatz and the similar ansatz for the test function v_N are substituted into the weak formulation. After further expanding the substituted expressions and executing the derivative operations on the known test and trial functions, this procedure yields a system of algebraic equations with N unknown coefficients α_k . Further application of boundary conditions, such as Dirichlet or Neumann boundary conditions, ensures the system's solvability.

2.5 Spectral Proper Orthogonal Decomposition

The objective of (S)POD is to find an approximation which represents the fluctuation energy of a mean-free flow field. This approximation is supposed to represent the flow field best in an energy sense. This requirement not only applies for SPOD, but also for POD [14]. In both, SPOD and POD, the flow field is considered as stochastic process

where so-called realizations of this process are taken [10]. In POD, one realization of this process is the state of the flow field at a certain point in time. When multiple of these realizations are taken into account, ordinary POD finds an approximation which is coherent wrt. the space, but neglects any temporal component in-between the realizations. SPOD overcomes this drawback and yields coherent approximations in space and time. The theoretical foundation for SPOD is outlined in the following and follows the theory outlined in Schmidt and Colonius [14].

Similar to POD, SPOD considers a mean-free flow field as stochastic process. However, in SPOD a mean-free realization $\mathbf{q}(\mathbf{x},t) = [u'_x(\mathbf{x},t), u'_r(\mathbf{x},t), u'_\theta(\mathbf{x},t)]^T$ of this stochastic process considers not only a realization at one point in time, but rather the realization over a period of time. Additionally, an ensemble of realizations is taken into account, which can be imagined as multiple runs of the same statistically independent experiment. The objective of SPOD is it to find an approximation $\chi(\mathbf{x},t)$ which is coherent in time and space, for all N realizations $\mathbf{q}_i(\mathbf{x},t)$ ($i \in \{0, \dots, N\}$), wrt. the energy. Formally, this objective yields the following optimization problem:

$$\max_{\chi(\mathbf{x},t)} \lambda = \frac{1}{N} \sum_{i=1}^N \frac{|\langle \mathbf{q}_i(\mathbf{x},t), \chi(\mathbf{x},t) \rangle|^2}{\langle \chi(\mathbf{x},t), \chi(\mathbf{x},t) \rangle} \quad (2.41)$$

where $\langle \langle \cdot, \cdot \rangle \rangle$ induces the spatio-temporal inner product

$$\langle \langle \mathbf{f}(\mathbf{x},t), \mathbf{g}(\mathbf{x},t) \rangle \rangle = \int_{-\infty}^{\infty} \int_{\Omega} \mathbf{f}^*(\mathbf{x},t) \mathbf{W}(\mathbf{x}) \mathbf{g}(\mathbf{x},t) d\Omega dt \quad (2.42)$$

for arbitrary functions \mathbf{f}, \mathbf{g} , where $\mathbf{W}(\mathbf{x})$ is an appropriate, diagonal weighting matrix and where the asterisk superscript denotes the complex-conjugate. Subsequently, the above optimization problem leads to the eigenvalue problem

$$\underbrace{\langle \langle N^{-1} \sum_{i=1}^N \mathbf{q}_i(\mathbf{x},t) \mathbf{q}_i^*(\mathbf{x}',t) dt, \chi(\mathbf{x}',t) \rangle \rangle}_{\mathbf{C}(\mathbf{x},\mathbf{x}',t,t')} = \lambda \chi(\mathbf{x},t) \quad (2.43)$$

where $\mathbf{C}(\mathbf{x},\mathbf{x}',t,t')$ is identified as the two-point space-time correlation tensor. However, for statistically stationary flows the correlation wrt. time rather depends on the temporal difference $\tau = t - t'$ of two points in time. Hence the correlation tensor can be transformed to $\mathbf{C}(\mathbf{x},\mathbf{x}',\tau)$ which enables the application of a Fourier transform

$$\mathbf{S}(\mathbf{x},\mathbf{x}',\omega) = \int_{-\infty}^{\infty} \mathbf{C}(\mathbf{x},\mathbf{x}',\tau) \exp(-i\omega\tau) d\tau \quad (2.44)$$

to transform the space-time correlation tensor to the so-called cross spectral density tensor. Finally, when multiplying the eigenvalue problem in eq. 2.43 with $\exp(-i\omega t)$, the final eigenvalue problem

$$\langle \mathbf{S}(\mathbf{x}, \mathbf{x}', \omega), \hat{\chi}(\mathbf{x}, \omega) \rangle = \lambda(\omega) \hat{\chi}(\mathbf{x}, \omega) \quad (2.45)$$

is obtained, where $\hat{\chi}(\mathbf{x}, \omega)$ is the eigenvector of the spectral eigenvalue problem and corresponds to $\chi(\mathbf{x}, t)$. $\langle \cdot, \cdot \rangle$ implies the inner product

$$\langle \mathbf{f}(\mathbf{x}, t), \mathbf{g}(\mathbf{x}, t) \rangle = \int_{\Omega} \mathbf{f}^*(\mathbf{x}, t) \mathbf{W}(\mathbf{x}) \mathbf{g}(\mathbf{x}, t) d\Omega \quad (2.46)$$

For a given discrete cross-spectral density tensor $\underline{\mathbf{S}}(\mathbf{x}, \mathbf{x}', \omega) \in \mathbb{C}^{N_x \times N_x}$, where N_x denotes the number of discrete points in the considered domain, the above eigenvalue problem yields

$$\underline{\mathbf{S}}(\mathbf{x}, \mathbf{x}', \omega) \underline{\mathbf{W}} \underline{\hat{\chi}}(\mathbf{x}, \omega) = \lambda(\omega) \underline{\hat{\chi}}(\mathbf{x}, \omega) \quad (2.47)$$

where the underline implies a discrete quantity, and is dropped again from now on. Hence, the solution of this discrete eigenvalue problem yields a set of N_x eigenvalue-eigenmode pairs for each frequency, where the eigenmode $\hat{\chi}(\mathbf{x}, \omega)$ displays a spatial structure oscillating at the frequency considered, and the eigenvalue $\lambda_i(\omega)$ represents the fluctuation energy incorporated by that particular mode.

SPOD has some characteristics worth mentioning. First, the $(\lambda_i(\omega), \hat{\chi}(\mathbf{x}, \omega))_i$ -pairs are sorted wrt. the eigenvalue, or the energy, respectively, meaning that the portion of energy incorporated by the modes decrease with increasing i . Second, the total fluctuation energy at one particular frequency is represented by the sum over all eigenvalues. Third, eigenmodes $\hat{\chi}(\mathbf{x}, \omega)_i$ and $\hat{\chi}(\mathbf{x}, \omega)_j$ are pairwise orthogonal for $i \neq j$ and hence build a basis for the oscillating flow field.

These properties of the SPOD are of high importance for the analysis in this study. Assuming the leading mode ($i = 1$) incorporates significantly more energy than modes with $i > 1$, it can be stated that the leading mode dominates the others energy-wise. Similar to the resolvent modes, such modes are said to exhibit low-rank behavior. Additionally, from the orthogonality-property it can be followed that this particular mode only occurs once and cannot be build by a linear combination of the remaining modes. This means that the flow is dominated by one mode and physically means that that there is one dominant mechanism present.

CHAPTER 3

Flow Configuration and Numerical Framework

This chapter outlines the numerical strategy followed by this study. It briefly presents the flow configuration and the LES for the reacting jet flow and shows representative data acquired from the LES which serves as input for both the SPOD and the linear framework. Subsequently, the numerical strategy for the linear framework as well as for the SPOD are presented. For detailed insights into the field of LES of reacting flows the reader is referred to Poinso and Veynante [48]

3.1 Large Eddy Simulation

For the analysis based on the linearized equations, valid mean fields are required to form the linear operators. One could assume that RANS computations would deliver satisfactory mean fields for the linear analysis. However, it was shown that the turbulent stresses affect the mean flow. Hence, to validly apply the linearized methods one relies on mean fields which display these effects. Furthermore, time resolved snapshots are required for the SPOD, where the unsteady LES also fulfills this requirement.

The equations governing a combustion process are transport equations for mass, momentum, energy and species. However, when turbulent flames are considered, the assumptions of constant pressure, equal diffusivity of heat and species, and adiabatic conditions lead to a transport equation governing a progress variable, which replaces the equations governing energy and species [48]. The progress variable is a scalar quantity ranging from 0 to 1, where 1 refers to the fully burnt gas. The governing equations can be formulated in a compact way such as

$$\partial_t \mathbf{q} = \mathcal{L}(\mathbf{q}) \quad (3.1)$$

which describes the non-linear system wrt. the state-vector \mathbf{q} incorporating the transported quantities. \mathcal{L} represents the non-linear operator. In the method of LES, the quantities are decomposed into

$$\mathbf{q} = \check{\mathbf{q}} + \mathbf{q}'' \quad (3.2)$$

In LES, the filtered quantities $\check{\mathbf{q}}$ are resolved by the grid, where the remaining part \mathbf{q}'' is unresolved and referred to as subgrid-scale(SGS) quantity. This decomposition, then, is substituted into eq. 3.1. For flows with inhomogeneous density, the Favre-filtered quantity is used to avoid density-velocity interactions when substituting the decomposition (Poinsot and Veynante [48]). A Favre-filtered quantity identifies as

$$\check{q} = \frac{1}{\bar{\rho}} \int_{-\infty}^{\infty} G(r)\rho(x-r)q(\mathbf{x}-\mathbf{r})dr \quad (3.3)$$

where $G(r)$ is an appropriate spatial filter function, such as a Gaussian. Then, the equations are filtered with the same filter function yielding the Favre-averaged equations

$$\partial_t(\bar{\rho}\check{\mathbf{q}}) = \check{\mathcal{L}}(\check{\mathbf{q}}) \quad (3.4)$$

where $\check{\mathcal{L}}$ is the non-linear operator altered due to the filtering.

LES aims to compute the Favre filtered quantities. However, the above filtering procedure reveals non-linear SGS-quantities, such as $\overline{\mathbf{u}''\mathbf{u}''}$. Similar to the terms arising when substituting the triple decomposition for the linearization (sec. 2.1), the terms arising here can be modeled analogously by the Boussinesq ansatz, where the unknown SGS-interactions are modeled by a proportionality with the Favre filtered fields in addition to a so-called subgrid-scale-viscosity ν_{SGS} . After substituting this LES-adopted ansatz into eq. 3.4, a model for the subgrid-scale viscosity is required.

In addition to the SGS-model, also a combustion model is required to model the heat release due to chemical reactions within the transport equation for the progress variable. For both the modeling of combustion and turbulence several different approaches with arbitrary complexity can be applied. The data obtained for this thesis is based on a turbulent flame speed model (TFC) closing the combustion model and a Smagorinsky model to closing the SGS-model. The computations were carried out by Zhang et al. [54]. For further information on the particular flow configuration of this thesis the reader is also referred to Zhang et al. [55].

Computations were carried out with OpenFOAM [56] with the following setup: The flow is simulated under atmospheric conditions, where a premixed methane-air mixture with an equivalence ratio of 0.9 is used. The global Reynolds number based on the nozzle diameter and the nozzle exit velocity on the jet axis is $15 \cdot 10^3$ for both the non-reacting and reacting jet flow. Figure 3.1 shows the instantaneous temperature and conversion rate of the progress variable indicating the instantaneous flame position. The inlet is on the far left hand side. After passing a convergent nozzle and a straight pipe the flow reaches the main nozzle's exit. Beside the main nozzle, there is an annular secondary injector which also operates on the premixed mixture and serves a pilot flame. Prior to this study, the simulation method was validated several times wrt. experiments such as in Nawroth et al. [57].

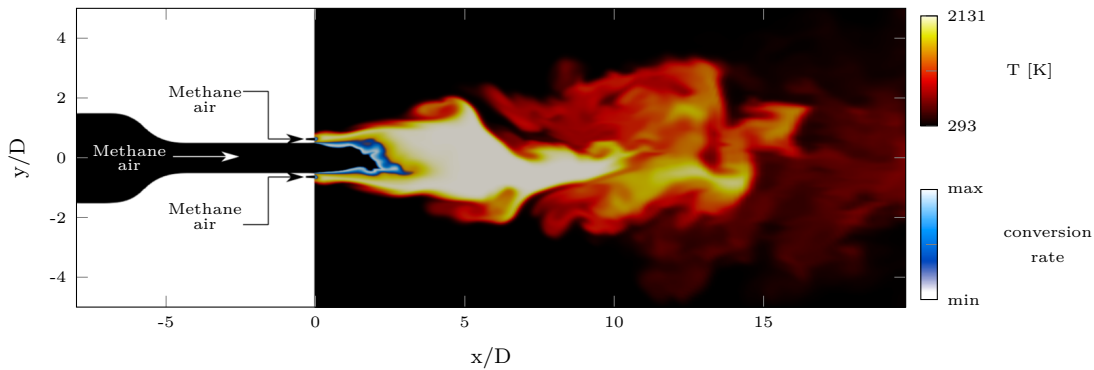


Figure 3.1: Instantaneous snapshot of the flame: black-to-yellow colormap displays instantaneous temperature field, white-blue-white colormap displays the conversion rate of the progress variable

3.2 Mean Flows and Time-Resolved Snapshots

Figure 3.2 presents the dimensionless temporal mean fields and instantaneous snapshots for the non-reacting and reacting jet flow obtained by the LES. Mean and instantaneous streamwise velocity fields of the non-reacting jet resemble ordinary characteristics of a turbulent jet. The maximum velocity is reached on the jet's centerline in the exit plane of the primary nozzle. The potential core approximately reaches $x = 5D$, where the velocity afterwards decays. In contrast to these observations, the reacting flow displays significantly different features. Figure 3.2 shows the temporal mean velocity and density fields (c,e) and a instantaneous snapshots of the streamwise velocity (d). Additionally, a contour line represents the mean position of the flame with

$$\bar{\mathbf{x}}_{Flame} = \mathbf{x} \left(\bar{T} = \frac{\bar{T}_{max} - \bar{T}_{min}}{2} \right) \quad (3.5)$$

Even though this measure seems rather rough, it gives a good first impression on the flame's influence on the flow. Up to the nozzle exit, non-reacting and reacting flow do not differ wrt. to the temporal mean. However, when the flow passes the region of chemical reactions, heat is released and the flow, subsequently, expands due to the heat release and the associated density drop of approximately one order of magnitude (fig. 3.2(e)). Thus, the maximum mean streamwise velocity is not reached within the nozzle's exit plane, as it is the case for the non-reacting flow, but rather at approximately $x = 2.5D$. Furthermore, the flow expands in radial direction and the shear layer thickness seems not to grow significantly before the velocity decreases again behind the maximum. The instantaneous profiles give a first impression of the dynamics. Where in the non-reacting configuration no significant structures occur, it looks as there are two, almost symmetric, vortical structures in the reacting snapshot. Nonetheless, this rather is an impression than

a solid observation.

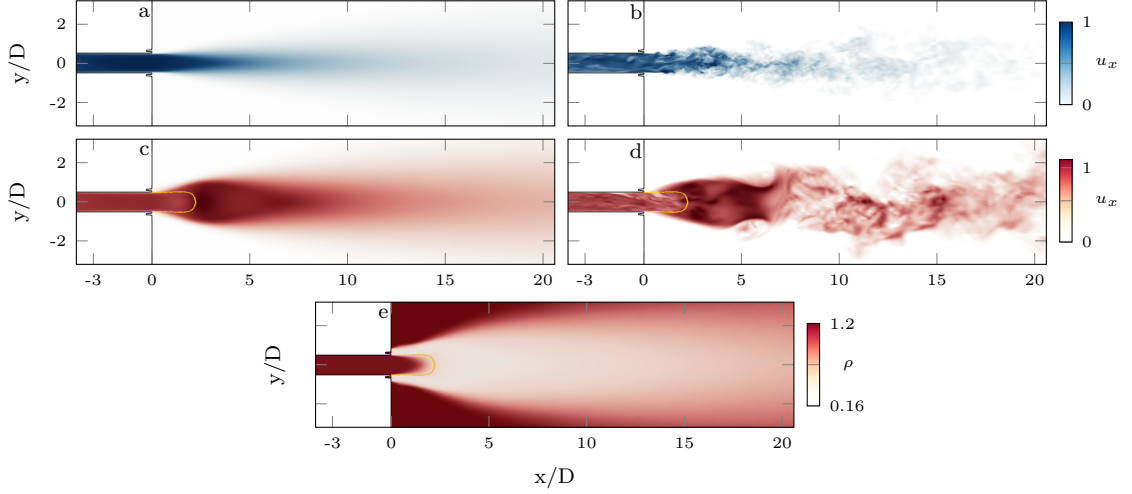


Figure 3.2: dimensionless LES- mean fields and snapshots: (a,b) temporal mean and instantaneous snapshot of the streamwise velocity of the non-reacting jet flow; (c,d) temporal mean and instantaneous snapshot of the streamwise velocity of the reacting jet flow; (e) temporal mean of the density of the reacting jet flow; orange contour within (c,d,e) represents the mean flame position \bar{x}_{Flame} determined by eq. 3.5

3.3 Spatial Discretization of the Linear Operators

Next, the fundamental approaches shown in sections 2.2 and 2.3 are further simplified and the numerical strategy is outlined explicitly for this study. The mean flows shown in section 3.2 are considered in cylindrical coordinates. Where chapter 2 assumed an arbitrary coordinate system, the cylindrical coordinate system has to be accounted for when discretizing the equations, i.e. the coordinate-specific derivative operators in eq. 2.19 and 2.20 have to be implemented. Furthermore, the azimuthal velocity component of the flow is zero, as it is typical for a round jet flow. All other remaining quantities are homogeneous wrt. to the azimuthal direction ($\partial_\theta q = 0$). This homogeneity in azimuthal direction allows to assume fluctuations to be harmonic wrt. to azimuthal direction such as

$$\hat{q}(x,r,\theta) = \tilde{q}(x,r) \exp(-i\omega t + im\theta) \quad (3.6)$$

Then, derivative operations for this ansatz yield

$$\partial_{x,r}\hat{q} = (\partial_{x,r}\tilde{q}) \exp(-i\omega t + im\theta) \quad \partial_\theta\hat{q} = im\tilde{q} \exp(-i\omega t + im\theta) \quad (3.7)$$

and crucially alter the linear system. m is the azimuthal wavenumber, where $m = 0$ results in axisymmetric fluctuations and $m = 1$ yields helical harmonic. These assumptions

lead to final equations representing our biglobal approach in the linear framework, enabling not only axisymmetric analysis, but also analysis for higher azimuthal wavenumbers. The full set of equations can be observed in Kaiser [30] in an expanded formulation. As

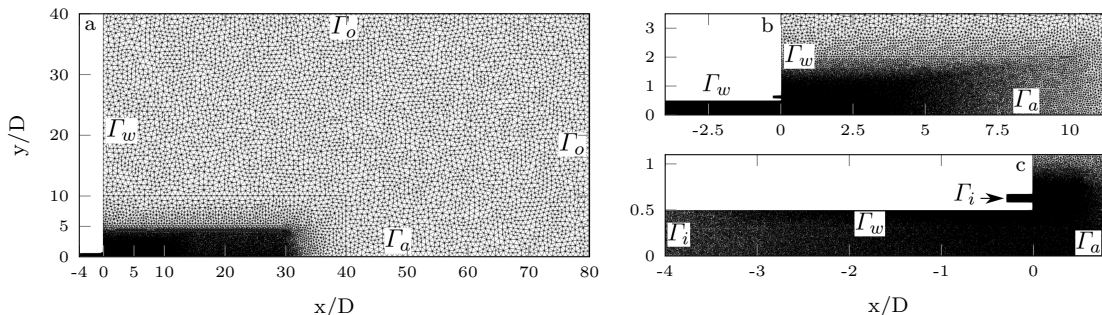


Figure 3.3: triangular discretization of the computational domain: (a) complete domain with $(x_{min}, x_{max}) = (-4, 80)D$ and $(r_{min}, r_{max}) = (0, 40)D$, (b) magnified view of the free shear flow region, (c) magnified view of the primary and secondary nozzle; Γ_i are the boundaries, where a, i, o, w denote the inlet, the axis, the outlet and the wall

already mentioned in chapter 2, the equations forming the linear operator require a spatial discretization. Figure 3.3 shows the grid for this discretization. Triangular elements were chosen which enable an adaptive grid resolution which does not depend on the grid structure. Due to the expectation of small perturbations, within the primary and secondary outlet, especially within the boundary layers, the triangular elements are chosen to be very small within this regions. Furthermore, regions where high shear is expected, e.g. regions adjacent to the potential core, have a high spatial resolution. With increasing downstream position, the mean field gradients decrease, such that the mesh resolution also decreases with the streamwise position.

To finally set up the linear operators for RA and LSA, the open source code FELiCS (**F**inite-**E**lement **L**inear **C**ombustion **S**olver) was used. FELiCS incorporates multiple linear analysis methods. Among others, the linear Low-Mach approach and the linear framework for non-reacting flows, from now on referred to as Cold-Flow approach, are implemented in cylindrical coordinates. For the discretization FELiCS applies the open source code FEniCS[58], which uses the FEM. As presented in section 2.4, the Galerkin method is employed to approximate the solution, where FELiCS chooses Lagrange polynomials as test and trial functions. To avoid instabilities, the Ladyzhenskaya-Babuska-Brezzi (LBB)-condition states that the order of pressure and velocity shape functions have to be unequal. Hence, FELiCS sets the order of two for the velocity and order one for the pressure Lagrange polynomials. Furthermore, the boundary conditions shown in table 3.1 are employed to the boundaries as presented in figure 3.3. The density is treated similarly as the pressure regarding the order of trial and test function and the treatment of the boundary conditions. For both the axisymmetric and first helical analysis the boundary conditions at the inlet, outlet and wall are the same. The boundary conditions at the

(symmetry-) axis have to be adapted corresponding to the azimuthal wavenumber.

Γ_a (m=0)	$\partial_{\mathbf{n}}\hat{u}_x = 0$	$\hat{u}_r = 0$	$\hat{u}_\theta = 0$	$\partial_{\mathbf{n}}\hat{p} = 0$	$\partial_{\mathbf{n}}\hat{p} = 0$
Γ_a (m=1)	$\hat{u}_x = 0$	$\partial_{\mathbf{n}}\hat{u}_r = 0$	$\partial_{\mathbf{n}}\hat{u}_\theta = 0$	$\hat{p} = 0$	$\hat{p} = 0$
Γ_i	$\hat{u}_x = 0$	$\hat{u}_r = 0$	$\hat{u}_\theta = 0$	$\hat{p} = 0$	$\hat{p} = 0$
Γ_i	$\hat{u}_x = 0$	$\hat{u}_r = 0$	$\hat{u}_\theta = 0$	$\hat{p} = 0$	$\hat{p} = 0$
Γ_w	$\hat{u}_x = 0$	$\hat{u}_r = 0$	$\hat{u}_\theta = 0$	$\partial_{\mathbf{n}}\hat{p} = 0$	$\partial_{\mathbf{n}}\hat{p} = 0$

Table 3.1: boundary conditions for the FE-discretized linear problem (RA & LSA); boundaries Γ_i as assigned in figure 3.3

For the RA, FELiCS follows the procedure of Garnaud et al. [35] to decompose the discretized resolvent operator and, subsequently, solves the discrete eigenvalue problem shown in eq. 2.32 for user-defined frequencies. After projecting the optimal forcing onto the resolvent operator, triplets of $(\mu(\omega), \hat{\phi}(\omega), \hat{\psi}(\omega))$ (gain, forcing, response) are obtained. For the LSA the discrete, direct and adjoint eigenvalue problems are formed as in eq. 2.27 and 2.34. The solution yields direct modes, adjoint modes and eigenvalue spectra. Prior to the main analysis, mesh convergence studies were performed for both the RA and LSA, where the presented grid in figure 3.3 showed results which were invariant against further mesh refinement.

3.4 Numerical Framework for Spectral Proper Orthogonal Decomposition

In section 2.5 it is seen that the objective of SPOD results in an eigenvalue decomposition of the cross-spectral density matrix \mathbf{S} . However, the derivation of the eigenvalue problem 2.47 is based on the infinitely long realizations of a stochastic process, which in reality is not possible. Hence, the spectral density must be approximated. This is accomplished by Welch's method. Furthermore, the specifics of the flow and data configuration can be taken into account. In the following the strategy applied to the specific configuration of this study is outlined and follows Schmidt and Colonius [14].

The time-resolved series of snapshots obtained from the LES are sampled on an unstructured grid similar as the one shown in figure 3.3 yielding the same advantages regarding the resolution as presented above. However, to decrease the computational load, a smaller domain size was chosen, which does not have a major impact on the SPOD results, because each snapshot realizes the correct boundary conditions naturally.

The theoretical foundations, outlined in section 2.5, consider an arbitrary stochastic process, neglecting any knowledge of the domain or the coordinate system. Since the snapshots $\mathbf{q}(\theta_k, t_j)$ are realized on N_θ azimuthal angles, first, the data is azimuthally Fourier decomposed such as

$$\mathbf{q}^m(t_j) = \frac{1}{N_\theta} \sum_{k=1}^{N_\theta} \mathbf{q}(\theta_k, t_j) \exp(im\theta_k) \quad (3.8)$$

where $\mathbf{q}(\theta_k, t_j) = [\mathbf{u}'_x, \mathbf{u}'_r, \mathbf{u}'_\theta]^T \in \mathbb{R}^{3N_x}$ is the flow's mean-free state-vector at one point in time $t_j \in \{1, \dots, N_t\}$. Each element of this vector incorporates the state of this element at each point in space ($\mathbf{x}_i, i \in \{0, \dots, N_x\}$), e.g. $\mathbf{u}'_x = [u'_x(\mathbf{x}_1), \dots, u'_x(\mathbf{x}_{N_x})]$. Due to the Shannon-Niuiquist theorem, eq. 3.8 results in $m \in \{0, \dots, N_{theta}/2\}$ unique azimuthally transformed snapshots, where $\mathbf{q}^m = \mathbf{q}^{-m}$ is assumed due to the jet's azimuthal homogeneity.

Second, the whole azimuthally transformed snapshot series \mathbf{q}^m of length N_t is split up into N_{seg} segments $\mathbf{q}_l^m(t_j)$ ($l \in \{1, \dots, N_{seg}\}$), each containing N_{DFT} snapshots, with an overlap of the segments of 80%. Subsequently each of this segments is Fourier transformed wrt. the time

$$\hat{\mathbf{q}}_l^m(\omega_k) = \frac{1}{N_{DFT}} \sum_{j=1}^{N_{DFT}} \mathbf{q}_l^m(t_j) \exp(-i\omega_k t_j) \quad (3.9)$$

where $j \in \{1, \dots, N_{DFT}\}$ and $\hat{\mathbf{q}}_l^m(\omega_k)$ is the azimuthally transformed frequency spectrum for each segment with discrete frequencies ω_k , where $\omega_k = k\omega_0$ and $\omega_0 = 2\pi/(N_{DFT}\Delta t)$. Then, for each azimuthal wavenumber and each discrete frequency, the data matrix

$$\mathbf{Q}_{\omega_k}^m = \left[\begin{array}{c|c|c|c|c} \hat{\mathbf{q}}_1^m(\omega_k) & \dots & \hat{\mathbf{q}}_l^m(\omega_k) & \dots & \hat{\mathbf{q}}_{N_{seg}}^m(\omega_k) \\ \hline \end{array} \right] \in \mathbb{C}^{N_x \times N_{seg}} \quad (3.10)$$

can be built, finally, leading to the approximation of the cross-spectral density

$$\mathbf{S}_{\omega_k}^m(\mathbf{x}, \mathbf{x}') = \frac{1}{N_{seg}} \mathbf{Q}_{\omega_k}^m \mathbf{Q}_{\omega_k}^{m \dagger} \quad (3.11)$$

where the \dagger -superscript denotes the hermitian-transposed in this case. This product accounts for two important steps. First, it implies a spatial correlation of the spectral data, and second, executes an ensemble average over all segments, i.e. the Welch-method of approximating spectral density.

Then, this approximation is built for each frequency ω_k and substituted into the eigenvalue problem stated in eq. 2.47. Furthermore, the weighting matrix \mathbf{W} is defined as

$$\mathbf{W}(\mathbf{x}) = \text{diag}([\mathbf{w}, \mathbf{w}, \mathbf{w}]) \quad w_i = \bar{\rho}_i r_i a_i \quad i \in 0, \dots, N_x \quad (3.12)$$

for the particular flow configuration studied within this thesis. r is the radius and a a weight representing the area surrounding each point in space. Hence, \mathbf{W} accounts for the distortion of a volume element due to the choice of cylindrical coordinates and for the varying cell size, as well as for the non-uniform density. An eigen-decomposition of the approximated spectral density and weight matrix ($\mathbf{S}\mathbf{W}$), finally, gives the solution to the SPOD-objective, the previously mentioned SPOD-eigenvalue-eigenmode-pairs $(\lambda(\omega_k), \hat{\chi}(\mathbf{x}, \omega_k))_i$, with $i \in \{1, \dots, N_x\}$ in descending order wrt. to the eigenvalue magnitude.

CHAPTER 4

Results - Spectral Proper Orthogonal Decomposition

The following chapter presents the flow dynamics obtained by the empirical mode decomposition, i.e. by the SPOD. For both non-reacting and reacting flow the results for axisymmetric (m^0) and first helical (m^1) analysis are presented. For each case, absolute eigenvalues as well as, from now on referred to as, relative eigenvalues are presented versus the dimensionless frequency $St = \frac{fD_{ref}}{u_{ref}}$. The relative spectra show the fraction of an eigenvalue on the sum of all eigenvalues at a particular frequency. Furthermore, the streamwise and radial components of the mode incorporating not the most energy absolutely, but relatively, are shown. First, the results for the non-reacting jet flow are discussed, then, for the reacting jet flow.

4.1 Non-Reacting Jet Flow

For the non-reacting flow, a total amount of 4800 snapshots with a sampling time of $\Delta t = 1$ ms is split up into segments with a window length of $N_{DFT} = 100$, resulting in a frequency resolution of $St_0 = 0.0473$. The snapshots are sampled on 4 distinct azimuthal positions. The rectangular domain considered for the SPOD is bounded by $(x_{min}, x_{max}) = (0, 40)D$ and $(r_{min}, r_{max}) = (0, 8)D$. Following the procedure outlined in section 3.4, the results, which are presented in the figures 4.1 and 4.2, are obtained for the m^0 -analysis and m^1 -analysis.

For the m^0 -analysis a monotonically decreasing absolute spectrum is obtained as expected (Fig. 4.1(a)). However, in the medium frequency regime where $St \in [0.3, 1.0]$, a noticeable elevation of the leading eigenvalue is observed. This behavior becomes even more distinct when the relative spectrum is considered, where the leading eigenvalue incorporates up to 8% of the total fluctuation energy at $St = 0.56$. Even though this seems not significant at first sight, the leading eigenvalue relatively incorporates twice as much energy as the second mode does at this frequency. Hence, the leading mode can be considered to exhibit a low-rank behavior. The corresponding dynamics can be observed in figure 4.1(b) and (d). They show the streamwise and radial component of the mode which relatively

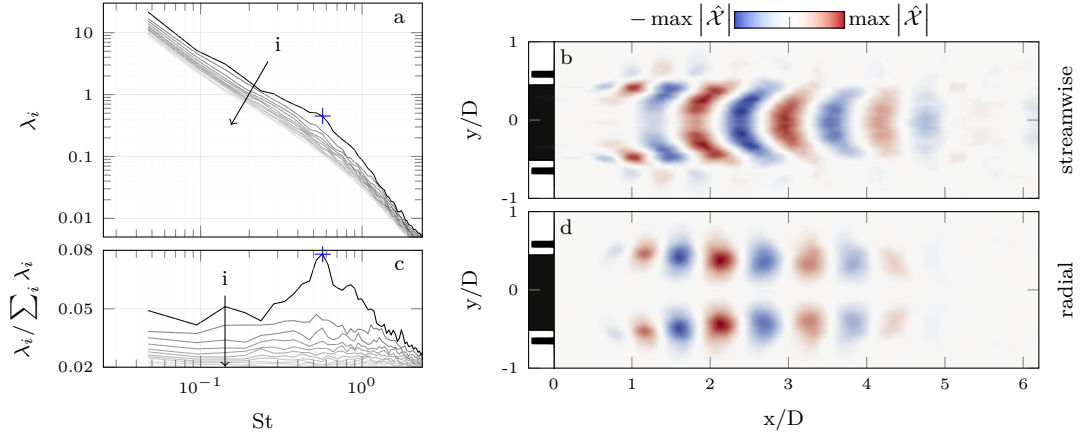


Figure 4.1: m^0 -SPOD-results for the non-reacting jet flow: (a) absolute, (c) relative eigenvalue spectrum, the shading of the curves represents the integral energy wrt. the frequency of the corresponding mode related to the integral of the leading mode, (b) streamwise component, (d) radial component at $St = 0.56$

incorporates the most energy. The wavepackets originate in the shear layer surrounding the jet potential core and evolve in downstream direction until they dissipate not far behind the jet potential core. Wavepackets at other frequencies within the low-rank regime show the same behavior, however, they differ wrt. to the wavelength from the wavepackets presented. Furthermore, their spatial amplitude distribution is more confined when higher frequencies are considered and more spread for lower frequencies. However, all these modes represent similar dynamics and are known as Kelvin-Helmholtz-type wavepackets which already have been observed in previous studies. Schmidt et al. [15] performed the same SPOD-analysis of a subsonic jet with a higher Re-number and find a similar elevation of the leading eigenvalue within the same frequency-regime. Instead of the streamwise velocity component, they present the coherent pressure mode. However, they resemble the same KH-type wavepackets as the results of this study.

Similar to the m^0 -analysis, the m^1 -analysis reveals the dominant modes. Figure 4.2 presents the dynamics similarly as before. Globally, the absolute spectrum (fig. 4.2(a)) does not differ much from the spectrum of the axisymmetric analysis. However, it is the relative spectrum (fig. 4.2(c)) which offers a better presentation of the eigenvalues. Same as in the axisymmetric case, an elevation of the leading eigenvalue is found for $St \in [0.3, 1]$. Furthermore, this elevation decreases similarly when approaching the upper bound ($St \rightarrow 1$). However, there are distinct differences between the spectra. First, the eigenvalue with the highest energy portion occurs at $St = 0.42$ and incorporates approximately 10%. Second, and even more striking is the difference for $St \rightarrow 0$. When approaching the lower limit, the leading mode does decrease compared to the largest separation, but instead of approaching the level of the second eigenvalue as it is the case for the m^0 -analysis, it preserves a certain elevation of the second eigenvalue at approximately

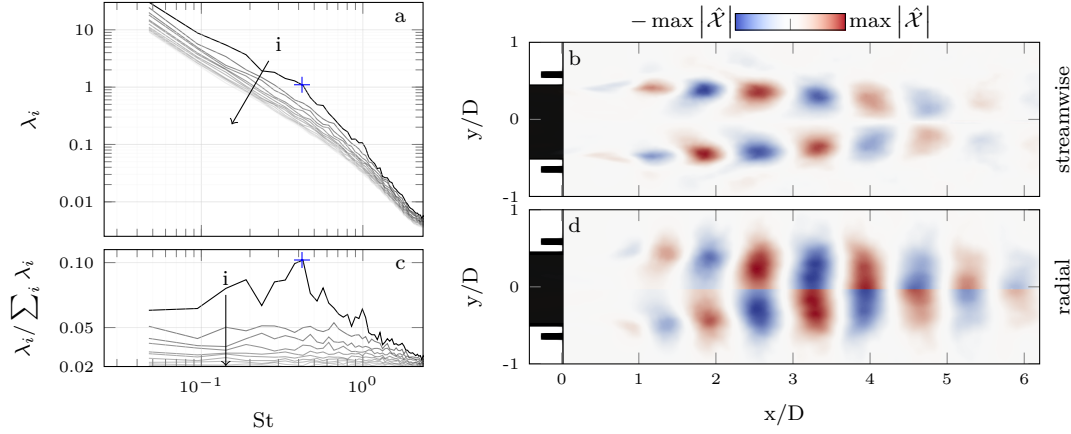


Figure 4.2: m^1 -SPOD-results for the non-reacting jet flow: (a) absolute, (c) relative eigenvalue spectrum, the shading of the curves represents the integral energy wrt. the frequency of the corresponding mode related to the integral of the leading mode, (b) streamwise component, (d) radial component at $St = 0.42$

7%. In general, the leading mode's relative energy is larger than in the axisymmetric case. The spatial structures which represent the low-rank behavior within the spectra are again represented by the mode with the most relative energy (fig. 4.2(b,d)). Although the terminology KH-type does not apply to the helical modes, they also evolve within the annular shear layer surrounding the potential core. Similar to the axisymmetric modes, the spatial spreading of the wavepackets increases with decreasing frequency. Typically for the first helical mode, the streamwise component is zero on the jet axis, where the radial component reaches high amplitudes on the centerline. Similar observations also were made in recently published literature for the helical modes. The observations within this study are in good agreement again with the findings of Schmidt et al. [15]. The same turbulent jet was investigated by Pickering et al. [17] for even smaller frequencies, where so-called streaks are identified. These streaks represent rot-like structures within the shear layer. However, within this study, the frequency resolution for $St \rightarrow 0$ does not suffice for such an analysis, but the agreement for the resolved frequency regime is rather good. However, for a thorough investigations of the effects for very low frequencies much more data is required, but is also not within the scope of this thesis. For this study it is sufficient to obtain the dynamics captured in fig. 4.2 and identify the leading effects to validate the linear framework results.

4.2 Reacting Jet Flow

In case of the reacting jet flow, 5600 snapshots are obtained from the LES with a sampling time of $\Delta t = 1$ ms. These are split up into segments with a length of $N_{DFT} = 250$ yielding a frequency resolution of $St_0 = 0.0189$. Snapshots are sampled on a rectangu-

lar (x,r) -plane with $(x_{min},x_{max}) = (0,30)D$ and $(r_{min},r_{max}) = (0,4.5)D$ on 12 distinct θ -positions. Similar as for the non-reacting configuration, the procedure in section 3.4 is followed. However, within the analysis for the reacting configuration the weighting-matrix accounts for the non-uniform density. Figures 4.3 and 4.4 show the results for the axisymmetric and helical analysis similar as for the non-reacting configuration. In contrast to the non-reacting flow, however, the mean flame position (eq. 3.5) is superposed.

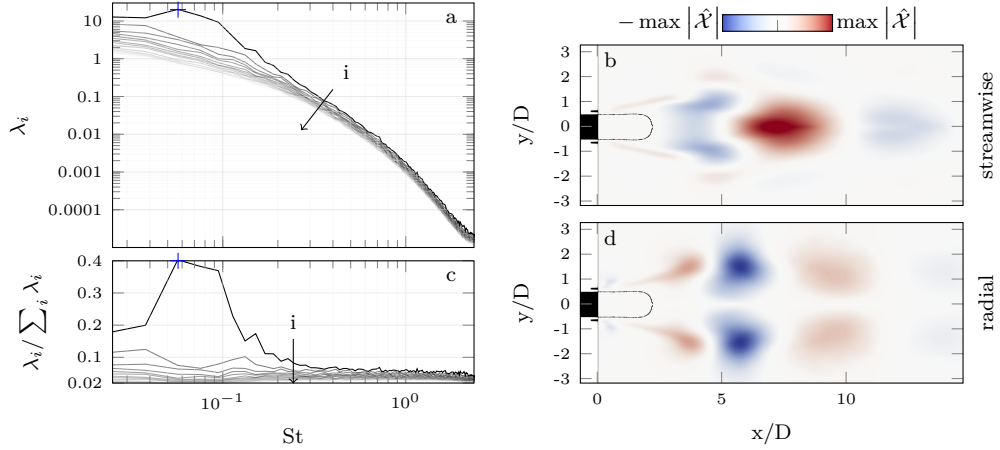


Figure 4.3: m^0 -SPOD-results for the reacting jet flow: (a) absolute, (c) relative eigenvalue spectrum, the shading of the curves represents the integral energy wrt. the frequency of the corresponding mode related to the integral of the leading mode, (b) streamwise component, (d) radial component at $St = 0.057$, black contour line in (b,d) indicates the mean flame position (eq. 3.5)

Figure 4.3 shows the absolute and relative spectra for the m^0 -analysis as well as the mode shapes representing the highest relative energy content. The absolute spectrum already presents distinct differences when compared to the non-reacting configuration. The absolute spectrum is not monotonically decreasing wrt. the frequency. The separation of the leading eigenvalue is significantly stronger, such that the absolute eigenvalue at $St = 0.057$ is higher as for lower frequencies. Additionally, the frequency regime where a strong separation occurs, shifts drastically to lower frequencies and is more narrow-banded such that the low-rank regime is identified within $St \in [0.056, 0.15]$. Within this regime the leading SPOD-mode is especially dominant. The relative spectrum identifies the leading mode's relative energy content upto 40%, significantly more than in the non-reacting flow, suggesting very dominant dynamics which are represented in fig. 4.3(b,d). Similar to the wavepackets for the non-reacting m^0 -analysis the wavepackets in the reacting jet flow originate in the shear layer surrounding the potential core. However, due to a flame being present the jet undergoes a spatial expansion, taking significant influence on the structure of the shear layer as it was observed in section 3.2. Although the wavepackets originate within the thin shear layer close to the flame, they cannot spatially spread within this

region. In fact, they do not spread before the shear layer reaches a sufficient thickness. However, when they do, they resemble KH-type wavepackets. First they are tilted with an angle against the main shear layer direction, but then adapt to this direction and further align with it. In addition to this, no wavepackets evolve upstream of the mean flame position. Similar observations are also made for the remaining modes within the low-rank regime.

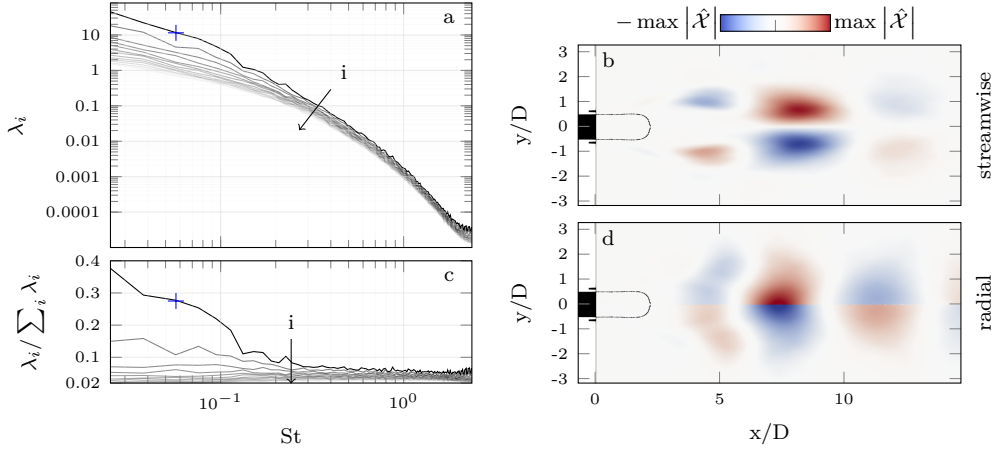


Figure 4.4: m^1 -SPOD-results for the reacting jet flow: (a) absolute, (c) relative eigenvalue spectrum, the shading of the curves represents the integral energy wrt. the frequency of the corresponding mode related to the integral of the leading mode, (b) streamwise component, (d) radial component at $St = 0.057$, black contour line in (b,d) indicates the mean flame position (eq. 3.5)

The results from the m^1 -analysis of the reacting jet flow are shown in figure 4.4. Despite the fact, that the low-rank behavior of the leading SPOD-mode is similarly significant as in the m^0 -analysis, a comparison of axisymmetric and helical analysis in the reacting configuration reveals similar effects as they are observed for the non-reacting jet flow. When moving along the frequency axis from higher to lower frequencies, the leading mode starts elevating at almost the same frequency as in the m^0 -spectra and rises to a significant separation. However the leading eigenvalue of the helical mode does not decrease when $St \rightarrow 0$ as the leading eigenvalue of the m^0 -analysis does. Considering a representative mode shape within the significant low-rank regime, similar wavepacket structures are identified as in the non-reacting m^1 -analysis. However, the influence of the flame on the wavepackets as discussed above transfer also onto the m^1 -modes. The flame significantly alters the shear layer such that the wavepackets do not spread before a certain shear layer thickness is reached.

Conclusion

m^0 -analysis as well as m^1 -analysis are performed for both the non-reacting and reacting jet flow and recover the most dominant flow dynamics. The dynamics for the non-reacting jet flow are well-known and are in good agreement with similar studies within recent publications. The analysis of the reacting jet flow dynamics suggest a similar form of behavior as in the non-reacting flow, only altered due to the expansion due to the flame. To the author's best knowledge, there are no similar results available within the published literature to compare to.

Regarding the analysis carried out, it would be beneficial to consider more data to obtain better-converged results and to resolve the spectra further into low-frequency regime. Furthermore, density fluctuations could be taken into account. However, the norm, i.e. the weighting matrix within eq. 3.12, would need modification. One suggestion is made by Lumley and Poje [59] by just normalizing the quantities with their respective variance. Another is given within the framework of Schmidt and Colonius [14], who suggest the compressible energy norm.

However, as it is one goal of this thesis to explore the underlying mechanisms with RA and LSA, the above analysis is sufficient to validate the dynamics obtained by the linear methods.

CHAPTER 5

Results - Linear Framework

Following the strategy outlined in chapter 1, the dynamics obtained by SPOD are now used to validate the linear framework. This validation not only refers to the choice of an appropriate eddy-viscosity model, but also to a comparison of the dynamics obtained by the SPOD to the dynamics revealed by the linear analysis methods for both non-reacting and reacting jet flow. Spectra from the SPOD-analysis are compared to the gain-spectra obtained by the RA. However, since they cannot be compared quantitatively, the trends are compared wrt. the low-rank regimes. The results from the linear framework are further investigated regarding the mechanisms causing the dominant dynamics.

The chapter is structured as follows: first the eddy-viscosity models are discussed, second, the RA for non-reacting jet is presented, third, results from the RA based on the Cold-Flow equations applied to the reacting baseflows are shown, and fourth, the RA based on the Low-Mach equations applied to the reacting jet flow is investigated. These results motivate, finally, the application and discussion of LSA to the reacting jet flow.

5.1 Eddy-Viscosity Model Evaluation

Four different eddy-viscosity models are introduced in section 2.1. Where the first two ν^0 and ν^1 , from now on referred to as ν^m -class, are rather simple, the third, the Semeraro-model (fig. 5.1), and the fourth, the TKE-model (fig. 5.2), are more sophisticated and take characteristic turbulent quantities into account. m^0 -RA-computations are performed based on the different eddy-viscosity models for the non-reacting jet. The RA-responses are visually compared to the SPOD-modes giving sufficient insights to choose a model for the subsequent analysis. However, first the spatially varying eddy-viscosities from the Semeraro and the TKE model are compared.

Figure 5.1 shows characteristic, turbulent quantities and the eddy viscosity for the Semeraro model. Figure 5.2 shows quantities which are relevant for the TKE-model and the resulting eddy-viscosity. When comparing the eddy-viscosity fields from Semeraro- to TKE-model, some differences can be identified. The first difference is that the TKE-model finds a vis-

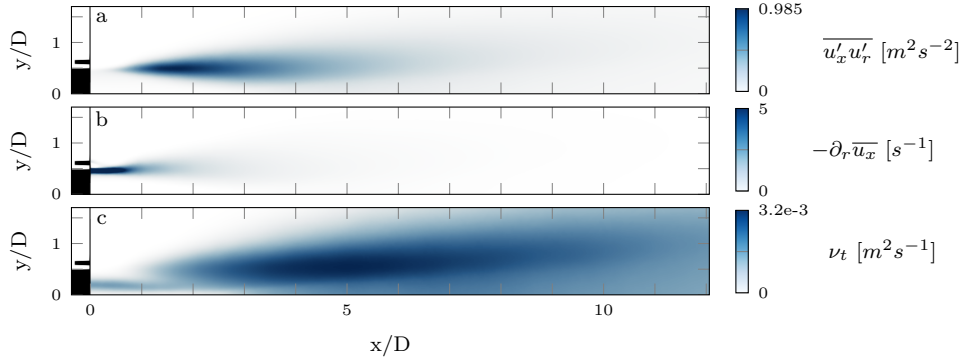


Figure 5.1: Characteristic flow quantities within the Semeraro eddy-viscosity model: (a) Reynolds-stress $\overline{u'_x u'_r}$; (b) mean strain rate $\partial_r \overline{u_x}$; (c) turbulent eddy-viscosity ν_t (eq. 2.21)

cosity almost equal to zero inside the jet's potential core, where the Semeraro-model finds the viscosity significantly larger than zero. This effect clearly arises due to the derivative approaching zero within the potential core (fig. 5.1(b)), despite the number ε avoiding a singularity in eq. 2.21. Another difference can be observed wrt. the magnitudes of ν_t , although the orders of magnitude are the same. Where the Semeraro model approaches its maximum approximately at $(x,r) = (5,0.5)D$, the eddy-viscosity computed with the TKE-model rises to its maximum further downstream on the jet centerline. The reason for this deviation is the interaction of Reynolds-stress and cross-stream derivative compared to the interaction of turbulent kinetic energy and characteristic length. Where the turbulent fluctuation quantities are rather similar, the derivative field and the characteristic length significantly differ. In fact it is the interaction of the almost vanishing derivative within the denominator of the Semeraro-model and the non-zero Reynolds-stress which causes the maximum of the eddy-viscosity. In contrast to that, the quotient-free TKE-model identifies a smooth characteristic length enabling a monotonous growth of the eddy viscosity with the streamwise position.

Figure 5.3 compares the RA-responses based on the different eddy-viscosity models to the SPOD-modes for $St = 0.59$. Considering the SPOD-mode, a distinct dissipation behavior of both the streamwise and radial components of the wavepackets can be observed. The RA-responses obtained with the models of the ν^m -class show a significantly different behavior, especially obvious for the streamwise component. In both ν^0 and ν^1 -model the modes preserve too far downstream. Furthermore, the response shapes do not suit the SPOD-mode shapes for downstream positions, even though the agreement is good within the jet's near field. Interestingly, no visually noticeable difference between ν^0 - and ν^1 -modell can be observed. The only difference between these two models can be observed wrt. their amplitudes which is not shown explicitly due to the dimensionless presentation. However, when the results are investigated, this statement holds for all relevant frequencies.

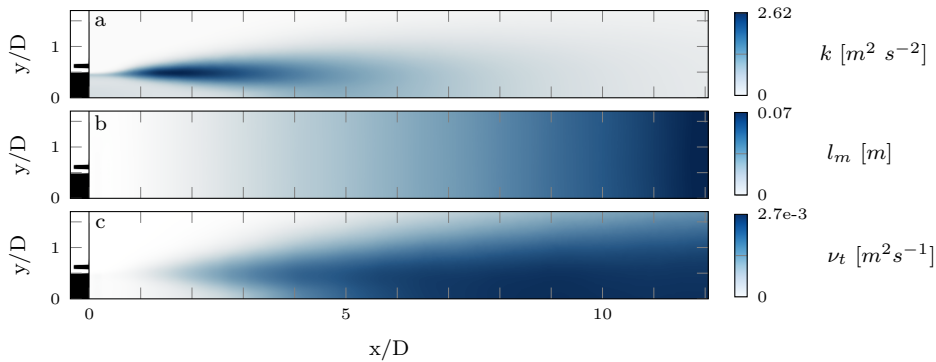


Figure 5.2: Characteristic flow quantities within the TKE eddy-viscosity model: (a) turbulent kinetic energy k ; (b) mixing length l_m ; (c) turbulent eddy-viscosity (eq. 2.23)

Furthermore the gain curves show only a difference in their magnitude, but not within their shapes. This observation suggests that the order of magnitude of the viscosity field is of less importance for an appropriate modeling of ν_t than it is the shape of the viscosity field. This again, suggests that the choice of the scaling constant of the TKE-model has minor influence on the results and leads to the two models remaining for the discussion. Both dissipation behavior as well as the shapes of the wavepackets further downstream drastically differ from the results obtained by the ν^m -models. It seems that the spatially varying ν_t -fields better account for an appropriate dissipation within the outer shear layer. However, concerning a comparison of Semeraro-model to TKE-model, the dissipation of the wavepackets obtained by the first seems too strong. Instead, the latter seems to capture the appropriate dissipation rate. The reason for this difference most probably originates from the above observations regarding the characteristic turbulent quantities and the resulting differences within the eddy-viscosity fields.

When comparing the streamwise and radial components for all models presented in figure 5.3, only difference concerning the component-specifics themselves are made out. Regarding wavelengths of x- and r-component there is no major difference. Additionally, the dissipation rate of radial and streamwise components seem to be the same. This observation makes the investigation of only one component necessary within the following analysis.

In fact, all the models presented are rather simple. However, these approaches try to model the stochastic velocity-velocity interactions with an approach mainly known from conventional CFD [49], even though the exact effect of these terms within the linear framework is still an open question where no favorable method is found yet. Finally, the TKE-model is chosen for all further analysis. Not only suit the RA-responses the SPOD-modes best, but also has the TKE-model the advantage of an easy implementation and of avoiding singularities.

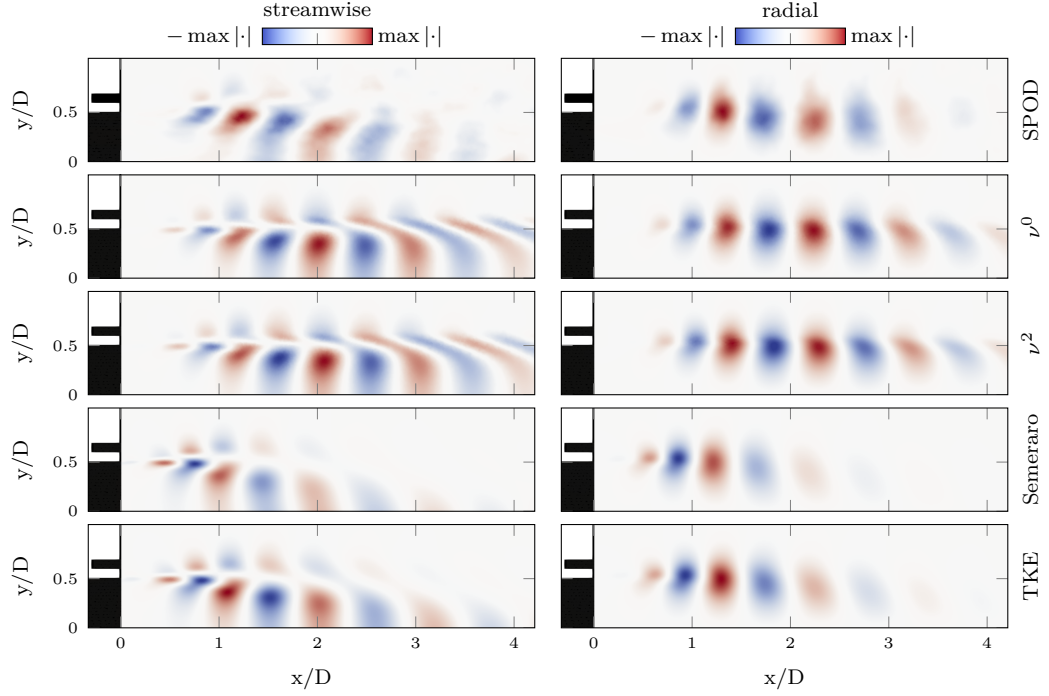


Figure 5.3: Eddy-viscosity-model evaluation: comparison of SPOD-mode and RA-responses at $St = 0.66$, the left row shows the streamwise components, the right shows the radial component; the first row shows the SPOD-mode where the underneath rows display the responses computed with the eddy-viscosity models as labeled on the right

5.2 Cold-Flow Resolvent Analysis of the Non-Reacting Jet Flow

The next section investigates the RA for the non-reacting jet flow. For the sake of brevity, only the streamwise components are compared from now on, if not mentioned otherwise. The results for the other components yield the same consequences for the following analysis.

RA-computations are performed for the same frequency domain as captured by the SPOD. Figure 5.4(a) shows a direct comparison between relative SPOD-spectrum and RA-gain. The leading gain curve separates from the sub-optimal gain curves in the same frequency regime as the SPOD does, meaning that the same frequency regime exhibits a low-rank behavior in the RA. The rise of the gain curves when $St \rightarrow 0$ is similarly observed in the absolute spectrum of the SPOD. However, the relative representation of SPOD-spectrum is chosen here, because the low-rank regime occurs more obvious when considered relatively. Nonetheless, the gain displays the same low-rank regime as the SPOD-eigenvalues, meaning that one dominant mechanism must be present. As described in section 2.2, this mechanism relates to a forcing-amplification-response mechanism. The RA-responses corresponding to the leading gain are shown in figure 5.4(e,f,g). These

RA-responses were chosen to represent the dynamics within the low-rank regime. They are compared to the SPOD-modes at the corresponding frequencies.

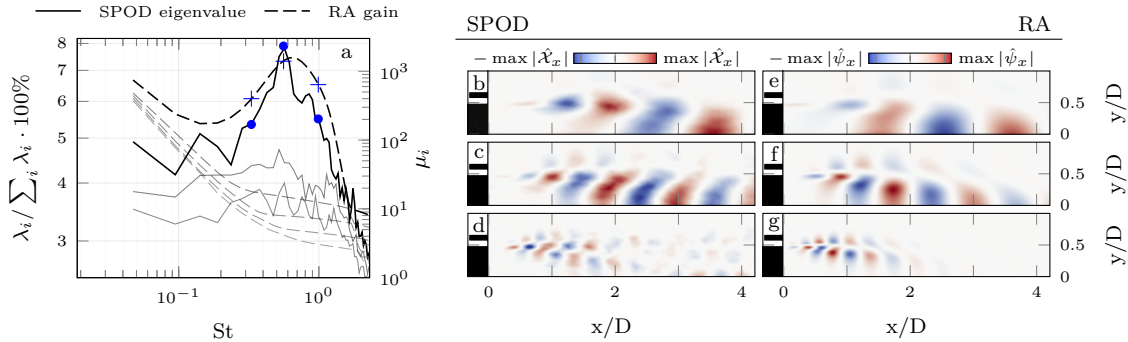


Figure 5.4: Comparison of m^0 -SPOD and -RA results for the non-reacting jet flow: (a) three leading relative SPOD-eigenvalues and 5 leading RA-gains, the shading of the curves represents the integrated quantity related to the leading mode; (b,c,d) leading streamwise SPOD-modes at $St = (0.33, 0.56, 0.99)$, (e,f,g) leading streamwise RA-responses at $St = (0.33, 0.56, 0.99)$

It can be seen, that the dynamics captured by the RA-responses are in good agreement with the SPOD-modes. As already observed in section 5.1, the dissipation behavior is captured well by the RA, wavelengths suit each other. However it also can be seen that the agreement is best where a distinct low-rank behavior is present, i.e. the dynamics match worse for $St = 0.33$ compared to $St = 0.56$ and $St = 0.99$.

An analogous comparison is presented in figure 5.5 for the m^1 -analysis. The RA-gain, again, displays the same low-rank behavior as the SPOD-spectrum does. It occurs in a similar frequency regime as the low-rank behavior in the m^0 -analysis. However, in contrast to the axisymmetric case, the separation preserves when approaching lower frequencies. Again, the rise of all gain-curves when $St \rightarrow 0$ results from the absolute presentation of the gain. The distance between leading and sub-optimal gain, however, stays approximately constant, similar to the behavior of the SPOD-eigenvalue.

The comparison of the m^1 -dynamics obtained from both methods shows a good agreement wrt. to the wavepackets shape. However, their amplitude development within the flow differ. The RA-responses reach their maximum further upstream than the SPOD-modes. This observation holds throughout the complete frequency range. Possible explanations for this mismatch could be to few snapshots or an insufficient resolution in azimuthal direction within the SPOD-analysis. However, the deviation between dynamics also could arise from the eddy-viscosity model. The influence of the eddy-viscosity on m^1 -fluctuations may differ from the influence on m^0 -fluctuations.

Finally, the flow dynamics captured by the RA-response are considered valid. Although, there are smaller deviations between SPOD-modes and RA-responses, the major features of the SPOD-modes are represented by the RA-responses. In fact, there are uncertain

parameters in both the SPOD as well as in the RA. More snapshots or further development concerning the eddy-viscosity model could lead to a even better agreement of the dynamics.

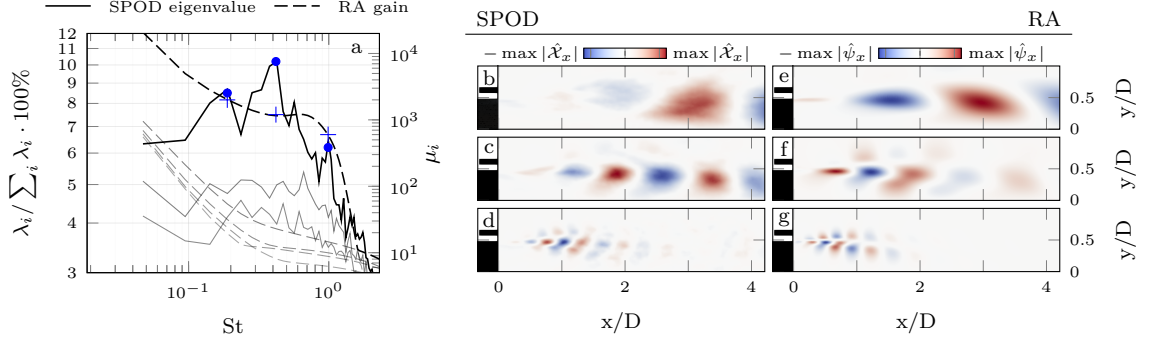


Figure 5.5: Comparison of m^1 -SPOD and -RA results for the non-reacting jet flow: (a) three leading relative SPOD-eigenvalues and 5 leading RA-gains, the shading of the curves represents the integrated quantity related to the leading mode; (b,c,d) leading streamwise SPOD-modes at $St = (0.19, 0.42, 0.99)$, (e,f,g) leading streamwise RA-responses at $St = (0.19, 0.42, 0.99)$

Since m^0 - and m^1 -RA are validly capturing the non-reacting jet flow dynamics, they now can be further analyzed. A major statement resulting from the RA is that if there is a low-rank behavior within the gain-spectra, there is one harmonic forcing to which the mean fields react in a particularly amplifying way. Figure 5.6 shows the harmonic forcing modes which cause the above presented response modes. All forcing modes are mainly confined to the boundary layer inside the primary nozzle. They occur as wall-adjacent wavepackets which grow in amplitude wrt. to increasing streamwise position, reaching the maximum amplitude close to the nozzle's exit edge. With increasing frequency the modes become more spatially confined at the exit edge for both m^0 - and m^1 -analysis. For both azimuthal wavenumbers, the forcing modes slightly tilt up and move into the beginning of the shear layer where they rapidly decay. Although forcing modes of both m^0 - and m^1 -analysis look alike, one has to keep the azimuthal dependency of the helical mode in mind.

In fact, it is exactly these structures which cause the flow dynamics represented by RA-reponses and SPOD-modes. Turbulent perturbations originate within the nozzle boundary layer, evolve and grow with downstream direction, until finally, they feed into the shear layer surrounding the jet potential core where they are amplified and result in the wavepackets represented by the response modes. This amplification, typically, applies to a broad frequency-regime as captured by both SPOD and RA and displays the amplifier characteristics of a turbulent jet. Similar dynamics have been obtained within recent studies. Garnaud et al. [35] obtain similar results for RA of a turbulent subsonic jet within their axisymmetric framework. They identify the same interaction between forcing and

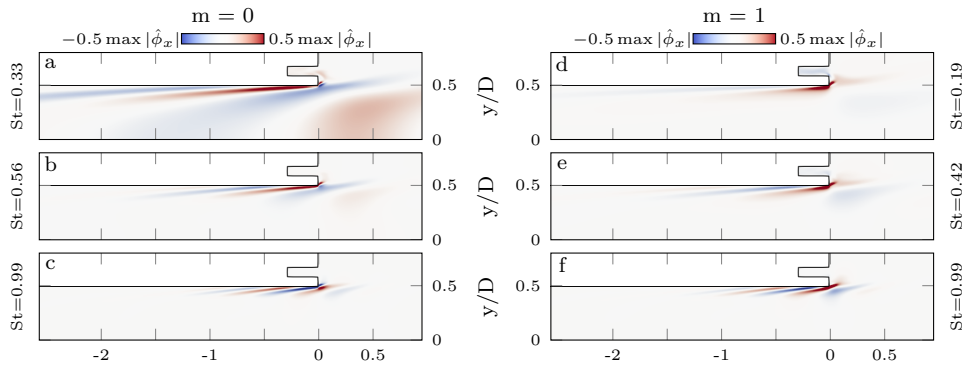


Figure 5.6: Optimal RA-forcing corresponding to the leading RA-responses presented in fig.5.4 and 5.5: left column: m^0 , right column: m^1 ; frequencies as indicated by labels on the side

response as described above and link it to the so-called Orr-mechanism. In case of the m^1 -framework, observations, similar to the above ones, have been made by Kaplan [60] who found the flow dynamics inside the nozzle boundary layer crucial for the wavepackets evolving the free shear region.

5.3 Cold-Flow Resolvent Analysis of the Reacting Jet Flow

This section presents results for the reacting jet flow. However, within this section, the RA based on the equations governing a uniform-density flow is applied to the reacting mean fields, i.e. to the mean velocity fields from the reacting flow only. It is referred to as Cold-Flow-RA in the following. Although this approach yields an unsatisfying agreement with the SPOD-results, it delivers important insights, especially, when comparing it to the results obtained by the Low-Mach-analysis. However, fulfilling only this one purpose, the analysis is carried out only within the axisymmetric framework.

Similar to the above comparison, figure 5.7(a) shows the relative SPOD-spectrum and the RA-gain wrt. the frequency, as well as a comparison of the SPOD-modes(b,c,d) to the RA-responses(e,f,g) for three characteristic frequencies.

The comparison of relative SPOD-eigenvalues and RA-gain, identifies significant differences. The trends do not coincide wrt. the frequency. The RA-gain exhibits a low-rank behavior at far higher frequencies than the SPOD-eigenvalue does. In fact, this deviation rises first doubts on the Cold-Flow-model applied to the reacting mean fields. However, it does not imply an incorrectness of the RA per se. Without a comparison of the mode shapes, the deviation wrt. to the low-rank regimes only implies that dominance of the leading mode wrt. optimal forcing does not coincide with dominance regarding the energy of the SPOD. Hence, the mode shapes are compared, where similarities between the SPOD- and RA-dynamics are observed. Although similarities of SPOD-modes and RA-responses

can be identified, the structure as well as the spatial confinement of the wavepackets differ significantly. The RA-response for $St = 0.23$ suggests coherent structures upstream of those identified by the SPOD at corresponding frequency. The overall structure of SPOD-mode and RA-response does not match for the frequency $St = 0.11$. Similar dissipation behavior can be identified within the modes for $St = 0.056$, but again, the modes lack agreement in the near field of the jet upto $x=5D$.

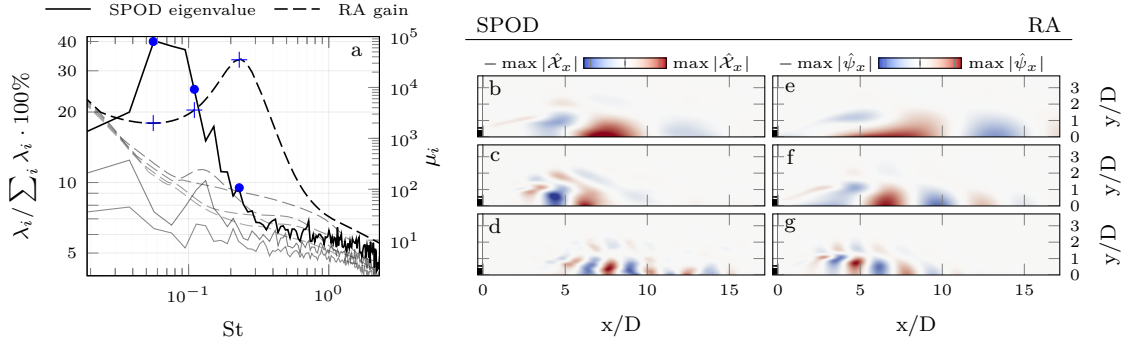


Figure 5.7: Comparison of m^0 -SPOD of the reacting jet flow and Cold-Flow-RA results for the reacting jet flow: (a) three leading relative SPOD-eigenvalues and 5 leading RA-gains, the shading of the curves represents the integrated quantity related to the leading mode; (b,c,d) leading streamwise SPOD-modes at $St = (0.056, 0.11, 0.23)$, (e,f,g) leading streamwise RA-responses at $St = (0.056, 0.11, 0.23)$

The above comparison presents the weakness of the Cold-Flow-RA when naively applied to reacting mean fields. However, it is worth to consider the RA-forcing modes. Later, when compared to the forcing of the Low-Mach-RA, they reveal further insights into the mechanisms responsible for the correct dynamics. Figure 5.8 shows the optimal forcing modes for the responses presented in figure 5.7. Similar to the forcing modes of the non-reacting jet, the forcing primarily is confined within the main nozzle and shows a similar wall-adjacent structure. Furthermore, it shows the same layered structure and a growing amplitude when approaching the nozzle exit in figure 5.8(b,c). This observation also holds for the forcing at $St = 0.056$, however, it is less confined, because the wavepackets grow in wavelength when lower frequencies are approached. Nonetheless, the forcing modes globally resemble the characteristics presented in section 5.2, i.e. growing perturbations within the nozzle's boundary layer. Especially, the mode at $St = 0.23$ which results in the highest amplification, resembles KH-type wavepackets in the response, and suggests that the Orr-mechanism is in place.

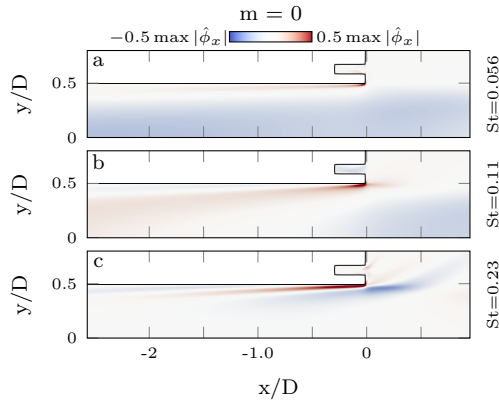


Figure 5.8: Optimal RA-forcing corresponding to the leading RA-responses presented in fig.5.7: frequencies as indicated by labels on the side

5.4 Low-Mach Resolvent Analysis of the Reacting Jet Flow

In the previous section it is seen that the Cold-Flow-RA fails to predict the correct dynamics, motivating a more sophisticated model. In fact, the linearized Low-mach equations, presented in section 2.1 (eq. 2.19), take the non-uniform density into account, and hence, represent the next step in modeling a flame being present. The following section presents the results from the RA based on this approach and discusses the significance of non-uniform density on the dynamics. Figure 5.9 shows the results of Low-Mach- m^0 -RA

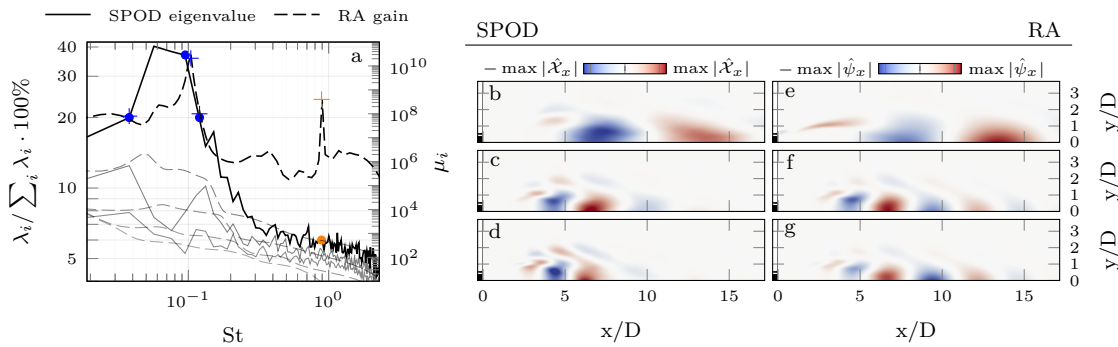


Figure 5.9: Comparison of Low-Mach- m^0 -RA and SPOD results for the reacting jet flow: (a) three leading relative SPOD-eigenvalues and 5 leading RA-gains, the shading of the curves represents the integrated quantity related to the leading mode; (b,c,d) leading streamwise SPOD-modes at $St = (0.038, 0.095, 0.113)$, (e,f,g) leading streamwise RA-responses at $St = (0.038, 0.10, 0.113)$, orange markers refer to fig. 5.11(a,b)

in comparison to the SPOD-results. The gain-spectrum changed significantly compared

to the Cold-Flow-RA for the reacting jet flow. Here, the most dominant gain is within the regime where the SPOD-eigenvalue exhibits the most dominant low-rank behavior. However, compared to the leading SPOD-eigenvalue, the gain is far more confined to a single frequency, peaking at approximately $St = 0.1$, upto multiple orders of magnitude higher than the remaining gain-spectrum. The subsequent falling flank suits the slope of the leading SPOD-eigenvalue. Furthermore, the RA-gain exhibits a significant low-rank behavior for $St > 0.15$, where the SPOD does not indicate any dominant structures. In fact, the RA yields non-physical results within this frequency domain and will be discussed later within this section. First, the focus is on the low frequency domain where SPOD-eigenvalue and gain coincide.

Besides the RA-response causing the significant peak within the gain spectrum ($St = 0.104$), one response at the beginning of the low-rank regime ($St = 0.038$) and one on the falling flank ($St = 0.113$) are compared to the corresponding SPOD-modes. Globally, the dynamics captured by SPOD and RA show a very good agreement. Small differences wrt. to the dissipation behavior of wavepackets further downstream most probably occur due to a wrongly predicted eddy-viscosity. Compared to the Cold-Flow-RA, the Low-Mach-RA obtains a significantly better alignment with the SPOD-modes within the whole low-rank regime. Especially, the the agreement between SPOD-mode at $St = 0.094$ and RA-response at $St = 0.104$ is striking.

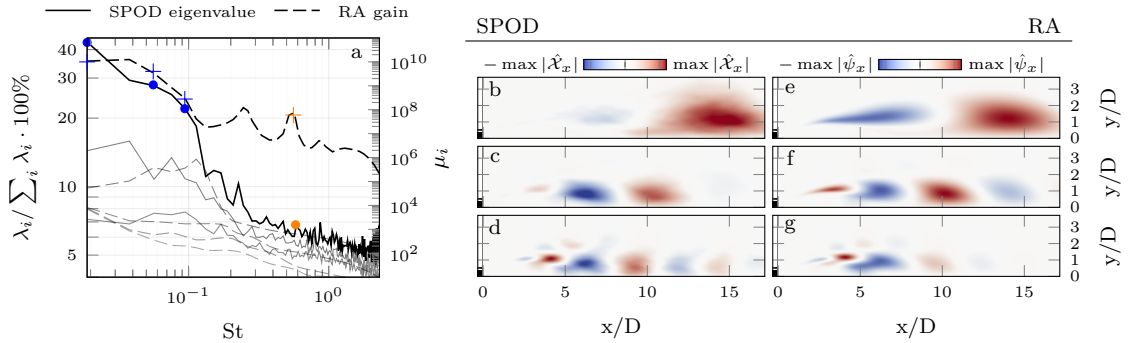


Figure 5.10: Comparison of Low-Mach- m^1 -RA and SPOD results for the reacting jet flow: (a) three leading relative SPOD-eigenvalues and 5 leading RA-gains, the shading of the curves represents the integrated quantity related to the leading mode; (b,c,d) leading streamwise SPOD-modes at $St = (0.019, 0.056, 0.094)$, (e,f,g) leading streamwise RA-responses at $St = (0.0189, 0.056, 0.094)$, orange markers refer to fig. 5.11(c,d)

A similar comparison for the Low-Mach- m^1 -RA is presented in figure 5.10. The trends of RA-gain suit those of the leading SPOD-eigenvalue especially well when $St \rightarrow 0$. However, similar to the m^0 -analysis, the gain exhibits a low-rank behavior at frequencies with $St > 0.15$ where the SPOD does not obtain any dominant eigenvalues.

Three RA-responses (fig. 5.10(e,f,g)) are compared to the dynamics obtained by SPOD (fig. 5.10(b,c,d)), representative for the low-rank regime at low frequencies. For all three

frequencies, the RA-responses display the SPOD-dynamics very well. Wavepackets display the same spatial structure in both cases, slight differences regarding the dissipation behavior occur. In fact, the dynamics agree better than in the m^1 -analysis of the non-reacting jet flow and support the conjecture of a lack of azimuthally sampled planes and too few snapshots in the non-reacting configuration.

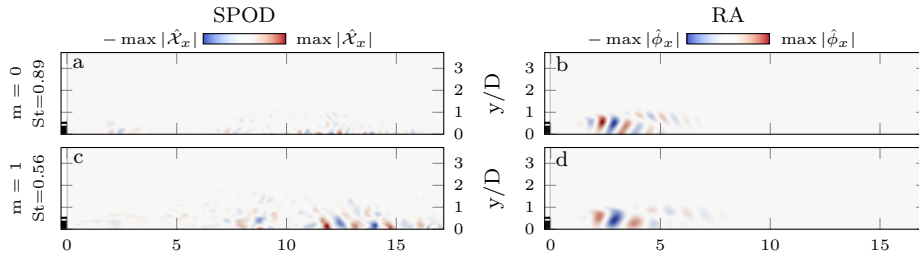


Figure 5.11: Comparison of m^0 - and m^1 -SPOD-modes to RA-responses labeled as non-physical: (a) m^0 , (c) m^1 -SPOD modes, (b) m^0 , (d) m^1 -RA-responses, frequencies as labeled on the left side, (a,b) refers to fig. 5.9, (c,d) to fig. 5.10

Next, the low-rank regimes for frequencies with $St > 0.15$ are considered for both m^0 - and m^1 -RA-analysis. For each, one representative response for this low-rank regime and the corresponding leading SPOD-mode are presented in figure 5.11. In both the axisymmetric and helical framework, the leading SPOD modes do not present any coherent wavepackets, suiting the non-existing low-rank behavior within the spectra. However, the RA-responses yield some kind of organized structures. To this point it is not clear why these structures occur. However, wavepackets of this shape are only observed in the Low-Mach-RA, not within the Cold-Flow-RA of the reacting jet flow, suggesting a correlation to the Low-Mach model. In fact, the linear Low-Mach equations are based on rather strong assumptions, e.g. no influence of the reaction kinetics and different species, or the assumption of constant gas properties such as the specific heat. Nonetheless, the model predicts the dynamics within the low-frequency regime extraordinarily well, such that the Low-Mach-RA is considered as valid within this domain. Instead, the behavior for higher frequencies is labeled as non-physical and ignored within the following analysis, also due to the fact that even though a low-rank behavior is exhibited, the magnitudes of the gain are at least one order smaller than the one observed within lower frequencies.

Figure 5.12 shows the optimal forcing responsible for the m^0 -responses in figure 5.9 and the m^1 -responses in figure 5.10. The forcing is spatially confined to the primary nozzle's exit edge, as well as to the secondary nozzle's outlet plane. Furthermore, there are no distinct difference between the forcing modes' structure regarding the frequency and the azimuthal wavenumber. In fact, one has to look very closely to identify differences between some of the forcing modes.

Compared to the forcing-modes obtained by the Cold-Flow-RA applied to the reacting base flows, the forcing modes obtained here, drastically differ, motivating the hypothesis

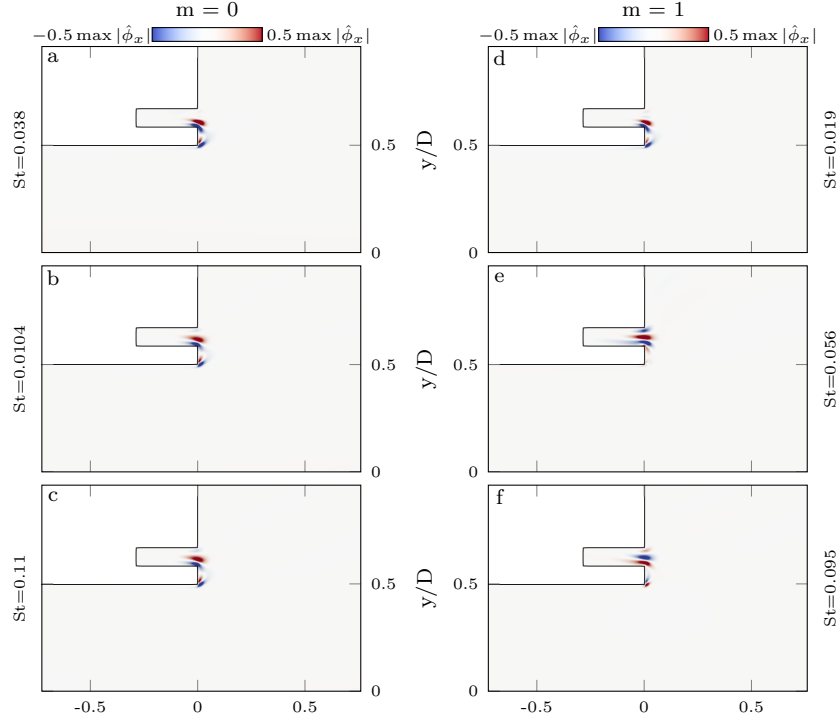


Figure 5.12: Optimal Low-Mach-RA-forcing corresponding to the leading RA-responses presented in fig.5.9 and 5.10: left column: m^0 , right column: m^1 ; frequencies as indicated by labels on the side

that the non-uniform density, accounted for by the Low-mach equations, has a significant impact. In fact, the forcing modes presented in figure 5.12 are localized where the density exhibits its highest gradients. That is where the pilot flame from the secondary nozzle and the main flame cause a drastic density drop.

Figure 5.13 shows the same forcing modes as they are presented in figure 5.12(b,e), only in a different window layout and under a different scaling of the magnitudes, and shows that forcing still exists within the main nozzle boundary layer. Although the magnitude of the forcing inside the boundary is of approximately two orders lower than it is in the confined region surrounding the nozzle exit, it shows that there are still perturbations existing. In fact, they resemble the same Orr-like mechanism as in the non-reacting jet flow. This observations suggest that the Orr-mechanism preserves, also in the reacting jet flow. Perturbations still exist and grow within the boundary layer, but when they approach the steep density gradients, they becomes amplified resulting in the spatially confined and two orders of magnitude stronger forcing amplitudes.

The observations of the discrete and high amplitude peak in the gain, the spatial location of the forcing mode and the identification of the density as driving cause for the prior

observations, motivate to consider the reacting flow's stability. In fact, studies of non-uniform density jet flows, regardless of what causes the non-uniform density, show that the flow's stability decreases when density gradients occur. Huerre and Monkewitz [37] investigated how non-uniform density affects the stability not only for a variety of flow configurations, but also for light jets and hot jets, by means of local LSA and found the density ratio as an important parameter driving instability. In addition to these observations, the significantly small banded and high amplitude peak in the RA-gain suggest a the reacting flow of this study also to exhibit at least a weakly dampened behavior such that a LSA is performed.

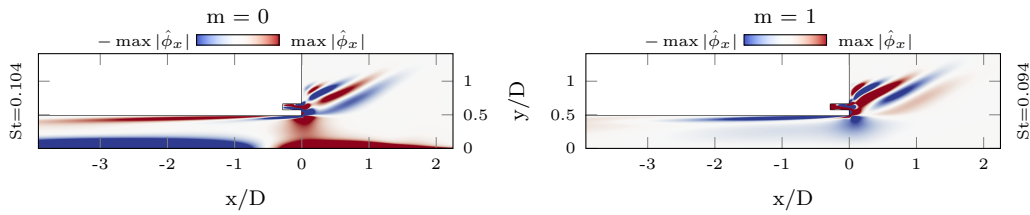


Figure 5.13: Optimal Low-Mach-RA-forcing corresponding to forcing modes presented in fig.5.12(b,f): presented in a different domain and with a different colormap scaling

5.5 Linear Stability Analysis of the Reacting Jet Flow

In the above section a distinct peak in the RA-gain is observed for the axisymmetric analysis, suggesting that the corresponding mode exhibits a very strong dominance. To further investigate this phenomenon, LSA is performed. LSA for the non-reacting jet flow is not carried out, as previous studies showed that non-reacting, turbulent jets do not exhibit any globally weakly dampened modes [35]. Furthermore, the gain-spectra for the non-reacting configuration do not exhibit such a narrow-banded and strong peak as it is the case for the reacting flow.

Figure 5.14 and 5.15 show the results for the LSA in the m^0 - and m^1 -framework. Globally, the spectra for both m^0 - and m^1 -analysis resemble a typical behavior for non-reacting turbulent jets, i.e. they identify decreasing eigenvalues wrt. the frequency. All of them have negative signs, meaning they have a negative growth rate. Nonetheless, certain eigenvalues are identified with a significant elevation from the residual spectrum. In fact, these modes could represent global weakly dampened modes. However, the same observation as in the Low-Mach-RA regarding non-physical behavior is made for modes with $St > 0.3$. Hence, these modes are not subject to further investigation. Additionally, the LSA-spectra are not computed to the same extent wrt. the frequency as the RA, because no dominant modes are expected for $St > 0$ unless they are non-physical. This leaves three modes for the m^0 -LSA and two modes for the m^1 -LSA open for discussion.

Figure 5.14 not only shows the global spectrum of the axisymmetric analysis, but also

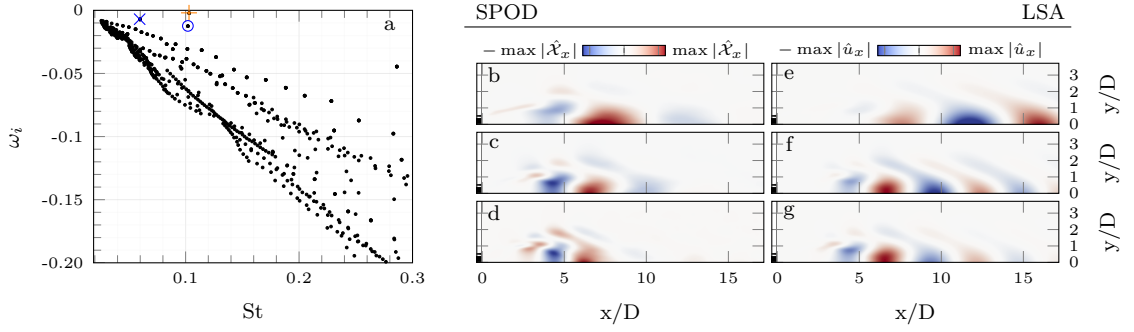


Figure 5.14: Comparison of Low-Mach- m^0 -LSA and SPOD results for the reacting jet flow: (a) LSA-eigenvalue spectrum, (b,c,d) leading streamwise SPOD-modes at $St = (0.056, 0.102, 0.103)$, (e,f,g) streamwise direct LSA-modes at $St = (0.056, 0.094, 0.113)$

shows the corresponding direct LSA-modes in comparison to the SPOD-modes with the closest frequencies. At first sight, the direct LSA modes resemble the same dynamics as captured by the SPOD. However, the amplitude development wrt. to the streamwise position only matches between the direct mode with $St = 0.103$ (fig. 5.14(g)) and the SPOD-mode at $St = 0.095$ (fig. 5.14(c)). One explanation for appearance of three less stable global modes could be the coupling of the system's boundaries with the modes. Lesshafft [61] has shown that reflections at the outflow-boundary can result in inaccurate predictions by the LSA, where the reflections are caused by a domain truncation and artificial boundary conditions. Waves are reflected by the outlet boundary, travel upstream and impact the direct modes, resulting in global, artificial feedback loop. This effect depends on the structures wavelength, and hence, on the frequency ω . However, setting the correct boundary conditions is a non-trivial problem within the global analysis. Neither Dirichlet-, nor Neumann-boundary conditions automatically fulfill the correct conditions. Within this study this effect is accepted. In fact, the analysis was performed under varying outlet conditions, where a sensitivity of all eigenvalues except the one at $St = 0.104$ was observed. Moreover, the modes at $St = 0.06$ (fig. 5.14(e)) and $St = 0.102$ (f) are observed to preserve further in streamwise position than the one at $St = 0.103$ (fig. 5.14(f)). When rescaling the modes amplitude it can be seen that the wavepackets preserve until reaching the outflow boundary, suiting the above described reflection phenomenon. The same holds for both modes in the m^1 -analysis. Assuming that these modes all have elevated eigenvalues due to the above described reflection phenomena and neglecting these modes, leaves only the m^0 -mode at $St = 0.103$, which even under scaling the amplitudes around numerical zero has no amplitudes traveling into the outlet boundary. Hence, it is the only mode being considered globally weakly damped.

Figure 5.16(a,b) shows the adjoint modes corresponding to this global mode. It presents that particular region where the flow is especially receptive wrt. external forcing, and hence, explains why the optimal forcing from the Low-Mach-RA is confined to that particular

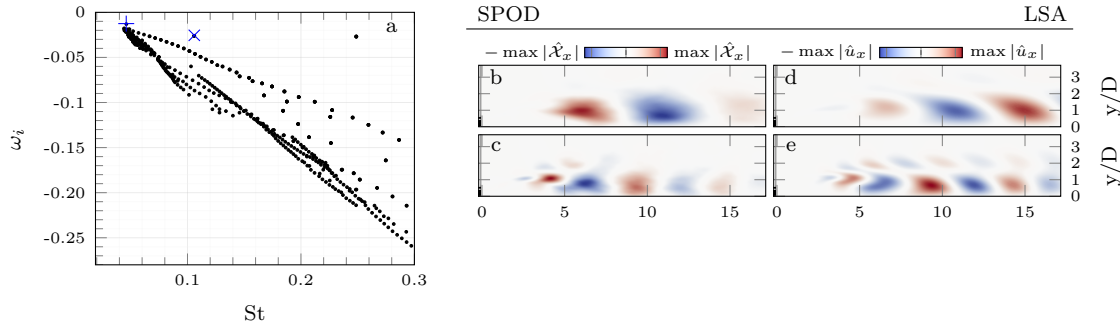


Figure 5.15: Comparison of Low-Mach- m^1 -LSA and SPOD results for the reacting jet flow: (a) LSA-eigenvalue spectrum, (b,c) leading streamwise SPOD-modes at $St = (0.046, 0.106)$, (d,e) streamwise direct LSA-modes at $St = (0.056, 0.094)$

region around the primary and secondary nozzles exit planes. However, in case LSA, the weakly damped mode results from an internal feedback mechanism and usually is caused by a confined region of absolute instability where this feedback is especially strong. Gianetti and Luchini [52] determine this origin region via a structural sensitivity analysis where the structural sensitivity is computed as presented in eq. 2.35. Regions of high structural sensitivity identify the origin of the global mode. An approximation of that structural sensitivity is presented in figure 5.16(c) where only the streamwise and radial components are taken into account. It presents the origin of the global mode as a small region close to the primary nozzle’s exit edge.

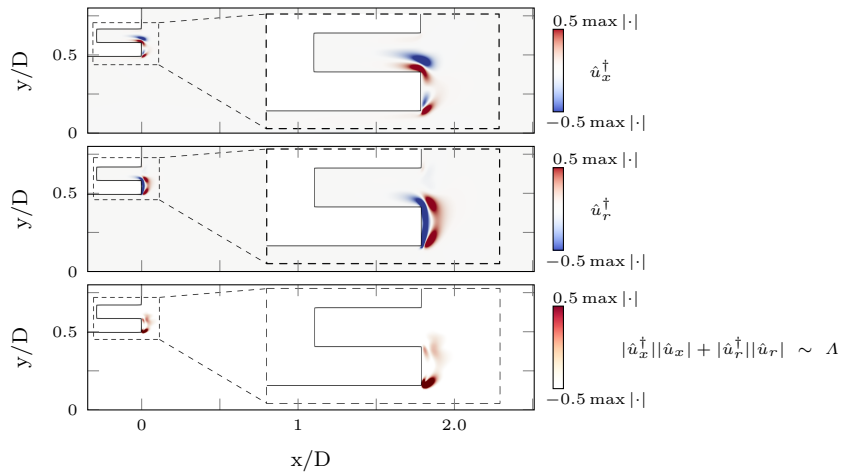


Figure 5.16: Adjoint LSA-modes of the Low-Mach-LSA at $St = 0.103$ and structural sensitivity approximation: (a) streamwise, (b) radial component of the adjoint mode, (c) structural sensitivity measure

Finally, the mechanism causing the strong amplification in the Low-Mach-RA is explained

by the LSA as a global weakly dampened mode. The origin of this mode is identified close to the nozzle exit edge as represented by the small pocket of high structural sensitivity. It is both, the region of highest shear gradients and highest density gradients due to the flame's presence. It suggests that the non-uniform density destabilizes the system and results in the flow's strong dynamics as they are captured in SPOD, RA and LSA. In fact, similar observation have been made in previous studies. Nichols et al. [39] find jets with variable density to exhibit absolute instability, and furthermore, determine a pocket near the nozzle exit as origin of the instability. Yu and Monkewitz [38] found that a lower density of high speed flow has a destabilizing effect. They come to the conclusion that the instability occurs not due to a new instability mechanism rather than a shift between stabilizing and destabilizing forces, suiting the results from this thesis where the Orr-mechanism also exists in the reacting jet flow, suggesting a similar mechanism as in non-reacting jet. However, the mechanism is brought out of balance due to the non-uniform density and results in a global mode.

CHAPTER 6

Conclusion

The goal of this study is to identify and investigate coherent structures in turbulent, non-reacting and reacting jet flows. Therefore, SPOD, RA and LSA are applied in a bi-global framework yielding axisymmetric as well as helical modes.

SPOD of the non-reacting jet flow identifies axisymmetric modes with moderate low-rank behavior within the intermediate frequency regime, and additionally, for zero-approaching frequencies in the helical framework. The dynamics of the reacting jet flow, however, exhibit a significantly stronger dominance of the leading mode and occur at lower frequencies within a narrower frequency band. The analysis methods based on the linear framework resemble the dynamics obtained by the SPOD for both the non-reacting as well as the reacting configuration. Hence, the linear framework methods are considered as valid and further investigated wrt. the underlying mechanisms.

First, Cold-Flow-RA is performed for the non-reacting jet flow. In good agreement to previous studies, the amplified KH-type wavepackets within the intermediate frequency regime and the corresponding Orr-mechanism within the nozzle boundary layer are recovered by the optimal response and forcing modes within the axisymmetric framework. Results for the helical analysis agree with the literature similarly well.

Second, Cold-Flow-RA is applied to the mean fields of the reacting jet flow. This approach does not capture the flow dynamics correctly due the equations neglecting any influence of the flame. In fact, one major influence is the abrupt rise in temperature and the associated density drop motivating the Low-Mach equations as suitable model to describe the dynamics.

Subsequently, the RA based on the Low-Mach equations is applied and captures the dynamics correctly. Most amplified responses coincide with most-energy incorporating structures within the low-frequency regime. The gain exhibits low-rank-behavior, including a distinct and narrow-banded peak suggesting a very strong mechanism being present. In

fact, the strong amplification behavior and the associated response dynamics are caused by an optimal forcing which is spatially confined and located where the mean density exhibits high gradients. Comparing these results to the naive application of the Cold-Flow-RA, additionally, reveals the significance of the non-uniform density for the dynamics of the reacting jet flow.

To further investigate the strong amplification identified by the RA, LSA was performed, and finally, explains the strong narrow-banded low-rank behavior obtained within the RA. One weakly dampened, global mode exists, which not only agrees well with the dynamics of the RA, but also frequency-wise with the peak in the RA-spectrum. An adjoint analysis shows that the flow is most receptive to perturbation close to the primary and secondary nozzle's exit planes, and explains the structure of the optimal RA-forcing. Furthermore, structural sensitivity presents a small pocket exhibiting absolute instability close to the primary nozzle's exit edge, and hence, locates the origin of the intrinsic mechanism.

All these observations are closely related to the non-uniform density field caused by the flame. In fact, they are not observed when neglecting the influence of non-uniform density. Yu and Monkewitz [38] found the density ratio of moving to ambient fluid to be a crucial parameter affecting the flow's stability. The observations of this thesis resemble this behavior. As the flow only exhibits an amplifier behavior within its non-reacting configuration, the combustion-associated density gradients cause the flow to exhibit a global weakly dampened mode. Modifications of the mean velocity fields due to the combustion related expansion were shown to have only minor effects, as the Cold-Flow-RA failed to capture the reacting jet flow dynamics. Further insights into the mechanism could be given by the baroclinic torque - a vorticity source due to misalignment of pressure and density gradients. For instance, Lesshafft and Huerre [62] identified the baroclinic torque as driver of instability within their heated jet flow. If this is equally the case in the configuration under investigation remains to be shown in future studies.

In conclusion, the goal of this thesis of identifying the coherent structures in turbulent jets was successfully met by all modal decomposition methods and for both the non-reacting and the reacting jet flow. Even more importantly however, is the investigation with the linear framework methods which allow to identify the driving mechanisms of flame dynamics in the configuration of a turbulent reacting jet flow.

Bibliography

- [1] Mansour Nasiri Khalaji. Investigation of Numerical Analysis Velocity Contours $k-\varepsilon$ Model of RNG , Standard and Realizable Turbulence for Different Geometries Investigation of Numerical Analysis Velocity Contours $k-\varepsilon$ Model of RNG , Standard and Realizable Turbulence for Different Geometries. (December), 2019.
- [2] Ann P. Dowling and Yasser Mahmoudi. Combustion noise. *Proceedings of the Combustion Institute*, 35(1):65–100, 2015. ISSN 15407489. doi: 10.1016/j.proci.2014.08.016.
- [3] *The Feynman Lectures on Physics, Vol. I: The New Millennium Edition: Mainly Mechanics, Radiation, and Heat*, volume 24. 2011. ISBN 9780465024933.
- [4] A.M. Jaffe. The millennium grand challenge in mathematics. *Notices of the American Mathematical Society*, 53(6), 2006. ISSN 00029920.
- [5] S. C. Crow and F. H. Champagne. Orderly structure in jet turbulence. *Journal of Fluid Mechanics*, 48(3):547–591, 1971. ISSN 14697645. doi: 10.1017/S0022112071001745.
- [6] Garry L. Brown and Anatol Roshko. On density effects and large structure in turbulent mixing layers. *Journal of Fluid Mechanics*, 64(4):775–816, 1974. ISSN 14697645. doi: 10.1017/S002211207400190X.
- [7] L Leylekian, M Lebrun, and P Lempereur. An Overview of Aircraft Noise Reduction Technologies. *AerospaceLab*, 1(7):1–15, 2014. doi: 10.12762/2014.AL07-01.
- [8] Kunihiko Taira, Steven L. Brunton, Scott T.M. Dawson, Clarence W. Rowley, Tim Colonius, Beverley J. McKeon, Oliver T. Schmidt, Stanislav Gordeyev, Vassilios Theofilis, and Lawrence S. Ukeiley. Modal analysis of fluid flows: An overview. *AIAA Journal*, 55(12):4013–4041, 2017. ISSN 00011452. doi: 10.2514/1.J056060.
- [9] Clarence W Rowley and Scott T M Dawson. Model Reduction for Flow Analysis and Control. (Dmd), 2017. doi: 10.1146/annurev-fluid-010816-060042.
- [10] John L. Lumley. *STOCHASTIC TOOLS IN TURBULENCE*. 1970.

-
- [11] Aaron Towne, Oliver T. Schmidt, and Tim Colonius. Spectral proper orthogonal decomposition and its relationship to dynamic mode decomposition and resolvent analysis. *Journal of Fluid Mechanics*, 847:821–867, 2018. ISSN 14697645. doi: 10.1017/jfm.2018.283.
- [12] Leandra Abreu, André Cavalieri, Philipp Schlatter, Ricardo Vinuesa, and Dan Henningson. SPOD and resolvent analysis of near-wall coherent structures in turbulent pipe flows. pages 1–20, 2020.
- [13] Leandra I. Abreu, André V.G. Cavalieri, Philipp Schlatter, Ricardo Vinuesa, and Dan Henningson. Wavepackets in turbulent flow over a NACA 4412 airfoil. *31st Congress of the International Council of the Aeronautical Sciences, ICAS 2018*, pages 1–10, 2018.
- [14] Oliver T. Schmidt and Tim Colonius. Guide to spectral proper orthogonal decomposition. *AIAA Journal*, 58(3):1023–1033, 2020. ISSN 00011452. doi: 10.2514/1.J058809.
- [15] Oliver T. Schmidt, Aaron Towne, Georgios Rigas, Tim Colonius, and Guillaume A. Brès. Spectral analysis of jet turbulence. *Journal of Fluid Mechanics*, 855(1971): 953–982, 2018. ISSN 14697645. doi: 10.1017/jfm.2018.675.
- [16] Petrônio A. Nogueira, André V. Cavalieri, Oliver T. Schmidt, Peter Jordan, Vincent Jaunet, Ethan Pickering, Georgios Rigas, and Tim Colonius. Resolvent-based analysis of streaks in turbulent jets. (May), 2019. doi: 10.2514/6.2019-2569.
- [17] Ethan Pickering, Georgios Rigas, Petrônio A. S. Nogueira, André V. G. Cavalieri, Oliver T. Schmidt, and Tim Colonius. Lift-up, Kelvin-Helmholtz and Orr mechanisms in turbulent jets. (August), 2019. ISSN 14697645. doi: 10.1017/jfm.2020.301.
- [18] Takeshi Shoji, Yuki Iwasaki, Kodai Kato, Seiji Yoshida, Shigeru Tachibana, and Takeshi Yokomori. Effects of Flame Structures on Direct Combustion Noise Produced by Lean-Premixed H₂/Air Low-Swirl Jet Flames . (January):1–22, 2020. doi: 10.2514/6.2020-0918.
- [19] W. C. Reynolds and A. K.M.F. Hussain. The mechanics of an organized wave in turbulent shear flow. Part 3. Theoretical models and comparisons with experiments. *Journal of Fluid Mechanics*, 54(2):263–288, 1972. ISSN 14697645. doi: 10.1017/S0022112072000679.
- [20] B. Marasli, J. Cohen, and V. Levinski. Mean flow distortion due to finite-amplitude instability waves in a plane turbulent wake. *Physics of Fluids*, 6(3):1315–1322, 1994. ISSN 10706631. doi: 10.1063/1.868299.
- [21] Vladislav Mantič-Lugo, Cristóbal Arratia, and François Gallaire. Self-consistent mean flow description of the nonlinear saturation of the vortex shedding in the cylinder wake. *Physical Review Letters*, 113(8):1–5, 2014. ISSN 10797114. doi: 10.1103/PhysRevLett.113.084501.

- [22] M. P. Juniper, O. Tammisola, and F. Lundell. The local and global stability of confined planar wakes at intermediate Reynolds number. *Journal of Fluid Mechanics*, 686(November):218–238, 2011. ISSN 00221120. doi: 10.1017/jfm.2011.324.
- [23] G. V. Iungo, F. Viola, S. Camarri, F. Porté-Agel, and F. Gallaire. Linear stability analysis of wind turbine wakes performed on wind tunnel measurements. *Journal of Fluid Mechanics*, 737:499–526, 2013. ISSN 14697645. doi: 10.1017/jfm.2013.569.
- [24] F. Viola, G. V. Iungo, S. Camarri, F. Porté-Agel, and F. Gallaire. Prediction of the hub vortex instability in a wind turbine wake: Stability analysis with eddy-viscosity models calibrated on wind tunnel data. *Journal of Fluid Mechanics*, 750:R1, 2014. ISSN 14697645. doi: 10.1017/jfm.2014.263.
- [25] Pedro Paredes, Steffen Terhaar, Kilian Oberleithner, Vassilis Theofilis, and Christian Oliver Paschereit. Global and Local Hydrodynamic Stability Analysis as a Tool for Combustor Dynamics Modeling. *Journal of Engineering for Gas Turbines and Power*, 138(2), 2016. ISSN 15288919. doi: 10.1115/1.4031183.
- [26] Kilian Oberleithner, Lothar Rukes, and Julio Soria. Mean flow stability analysis of oscillating jet experiments. *Journal of Fluid Mechanics*, 757(July):1–32, 2014. ISSN 14697645. doi: 10.1017/jfm.2014.472.
- [27] Yan Ding and Mutsuto Kawahara. Three-dimensional linear stability analysis of incompressible viscous flows using the finite element method. *International Journal for Numerical Methods in Fluids*, 31(2):451–479, 1999. ISSN 02712091. doi: 10.1002/(SICI)1097-0363(19990930)31:2<451::AID-FLD885>3.0.CO;2-O.
- [28] Guillaume A. Brès and Tim Colonius. Three-dimensional linear stability analysis of cavity flows. *Collection of Technical Papers - 45th AIAA Aerospace Sciences Meeting*, 19(January):13594–13609, 2007.
- [29] Asei Tezuka and Kojiro Suzuki. Three-dimensional global linear stability analysis of flow around a spheroid. *AIAA Journal*, 44(8):1697–1708, 2006. ISSN 00011452. doi: 10.2514/1.16632.
- [30] Thomas L. Kaiser. Impact of Flow Rotation on Flame Dynamics and Hydrodynamic Stability, 2019.
- [31] Lothar Rukes, Christian Oliver Paschereit, and Kilian Oberleithner. An assessment of turbulence models for linear hydrodynamic stability analysis of strongly swirling jets. *European Journal of Mechanics, B/Fluids*, 59:205–218, 2016. ISSN 09977546. doi: 10.1016/j.euromechflu.2016.05.004.
- [32] J Nichols and S Lele. Global mode analysis of turbulent high-speed jets. *Annual Research Briefs*, 2010.

- [33] David G. Crighton and M. Gaster. Stability of slowly diverging jet flow. *Journal of Fluid Mechanics*, 77(1976):397–413, 1976.
- [34] Alison J. Cooper and David G. Crighton. Global modes and superdirective acoustic radiation in low-speed axisymmetric jets. *European Journal of Mechanics, B/Fluids*, 19(5):559–574, 2000. ISSN 09977546. doi: 10.1016/S0997-7546(00)90101-8.
- [35] X Garnaud, L Lesshafft, P J Schmid, and P Huerre. The preferred mode of incompressible jets : linear frequency response analysis. pages 189–202, 2013. doi: 10.1017/jfm.2012.540.
- [36] Christian Oliver Paschereit, Steffen Terhaar, Bernhard ČOSIĆ, and Kilian Oberleithner. Application of linear hydrodynamic stability analysis to reacting swirling combustor flows. *Journal of Fluid Science and Technology*, 9(3):JFST0024–JFST0024, 2014. ISSN 1880-5558. doi: 10.1299/jfst.2014jfst0024.
- [37] P Huerre and P A Monkewitz. Local and global instabilities in spatially developing flows. *Annual Review of Fluid Mechanics*, 22(1):473–537, 1990. doi: 10.1146/annurev.fl.22.010190.002353.
- [38] Minghuei Yu and Peter A Monkewitz. The effect of nonuniform density on the absolute instability of two dimensional inertial jets and wakes two-dimensional inertial jets and wakes. 1175, 1990. doi: 10.1063/1.857618.
- [39] Joseph W. Nichols, Peter J. Schmid, and James J. Riley. *Self-sustained oscillations in variable-density round jets*, volume 582. 2007. ISBN 0022112007005. doi: 10.1017/S0022112007005903.
- [40] Lloyd N. Trefethen, Anne E. Trefethen, Satish C. Reddy, and Tobin A. Driscoll. Hydrodynamic stability without eigenvalues. *Science*, 261(5121):578–584, 1993. ISSN 00368075. doi: 10.1126/science.261.5121.578.
- [41] Antonios Monokrousos, Espen Åkervik, Luca Brandt, and Dan S. Henningson. *Global three-dimensional optimal disturbances in the Blasius boundary-layer flow using time-steppers*, volume 650. 2010. ISBN 0022112009993. doi: 10.1017/S0022112009993703.
- [42] Denis Sipp and Olivier Marquet. Characterization of noise amplifiers with global singular modes: The case of the leading-edge flat-plate boundary layer. *Theoretical and Computational Fluid Dynamics*, 27(5):617–635, 2013. ISSN 14322250. doi: 10.1007/s00162-012-0265-y.
- [43] Thomas Ludwig Kaiser, Lutz Lesshafft, and Kilian Oberleithner. Prediction of the Flow Response of a Turbulent Flame to Acoustic Perturbations Based on Mean Flow Resolvent Analysis. *Journal of Engineering for Gas Turbines and Power*, 141(11), nov 2019. ISSN 0742-4795. doi: 10.1115/1.4044993.

-
- [44] Samir Beneddine, Denis Sipp, Anthony Arnault, and Julien Dandois. Conditions for validity of mean flow stability analysis. pages 485–504, 2016. doi: 10.1017/jfm.2016.331.
- [45] Georgios Rigas, Ethan M. Pickering, Oliver T. Schmidt, Petrônio A. Nogueira, André V. Cavalieri, Guillaume A. Brès, and Tim Colonius. Streaks and coherent structures in jets from round and serrated nozzles. (May), 2019. doi: 10.2514/6.2019-2597.
- [46] Ethan M. Pickering, Georgios Rigas, Denis Sipp, Oliver T. Schmidt, and Tim Colonius. Eddy viscosity for resolvent-based jet noise models. (May), 2019. doi: 10.2514/6.2019-2454.
- [47] Samir Beneddine, Robin Yegavian, Denis Sipp, and Benjamin Leclaire. Unsteady flow dynamics reconstruction from mean flow and point sensors: An experimental study. *Journal of Fluid Mechanics*, 824:174–201, 2017. ISSN 14697645. doi: 10.1017/jfm.2017.333.
- [48] Thierry Poinsot and Denis Veynante. *Theoretical and Numerical Combustion*, volume 3. R.T. Edwards Inc., 2012.
- [49] Stephan B. Pope. *Turbulent flows*. Cambridge Univ. Press, 2000.
- [50] Onofrio Semeraro, Lutz Lesshafft, Vincent Jaunet, and Peter Jordan. Modeling of coherent structures in a turbulent jet as global linear instability wavepackets : Theory and experiment. *International Journal of Heat and Fluid Flow*, 0:1–9, 2016. ISSN 0142-727X. doi: 10.1016/j.ijheatfluidflow.2016.10.010.
- [51] B. J. McKeon and A. S. Sharma. A critical-layer framework for turbulent pipe flow. *Journal of Fluid Mechanics*, 658:336–382, 2010. ISSN 00221120. doi: 10.1017/S002211201000176X.
- [52] Flavio Gianetti and Paolo Luchini. Structural sensitivity of the first instability of the cylinder wake. 581(May 2007):167–197, 2007. ISSN 00221120. doi: 10.1017/S0022112007005654.
- [53] Eric B. Becker, F.Graham Garcy, and J. Tinsley Oden. *Finite elements. An Introduction*. I edition.
- [54] F. Zhang, P. Habisreuther, M. Hettel, and H. Bockhorn. Modelling of a premixed swirl-stabilized flame using a turbulent flame speed closure model in les. *Flow, Turbulence and Combustion*, 82(4):537–551, 2009. ISSN 13866184. doi: 10.1007/s10494-008-9175-x.
- [55] Feichi Zhang, Thorsten Zirwes, Peter Habisreuther, Henning Bockhorn, Dimosthenis Trimis, Holger Nawroth, and Christian O Paschereit. Impact of Combustion Modeling on the Spectral Response of Heat Release in LES Impact of Combustion Modeling on

- the Spectral Response of Heat Release in LES. *Combustion Science and Technology*, 00(00):1–21, 2018. ISSN 0010-2202. doi: 10.1080/00102202.2018.1558218.
- [56] OpenFOAM. *OpenFOAM - The Open Source CFD Toolbox - User's Guide*, 2014.
- [57] Holger Nawroth, Christian Oliver Paschereit, Feichi Zhang, Peter Habisreuther, and Henning Bockhorn. Flow investigation and acoustic measurements of an unconfined turbulent premixed jet flame. *43rd Fluid Dynamics Conference*, pages 1–15, 2013. doi: 10.2514/6.2013-2459.
- [58] Martin S. Alnæs, Jan Blechta, Johan Hake, August Johansson, Benjamin Kehlet, Anders Logg, Chris Richardson, Johannes Ring, Marie E. Rognes, and Garth N. Wells. The fenics project version 1.5. *Archive of Numerical Software*, 3(100), 2015. doi: 10.11588/ans.2015.100.20553.
- [59] John L. Lumley and Andrew Poje. Low-dimensional models for flows with density fluctuations. *Physics of Fluids*, 9(7):2023–2031, 1997. ISSN 10706631. doi: 10.1063/1.869321.
- [60] Oguzhan Kaplan. Nozzle boundary-layer dynamics and wavepackets in subsonic turbulent jets, 2019.
- [61] Lutz Lesshafft. Artificial eigenmodes in truncated flow domains. *Theoretical and Computational Fluid Dynamics*, 2017. ISSN 1432-2250. doi: 10.1007/s00162-017-0449-6.
- [62] Lutz Lesshafft and Patrick Huerre. Linear impulse response in hot round jets. *Physics of Fluids*, 19(2):1–12, 2007. ISSN 10706631. doi: 10.1063/1.2437238.